2024

Application of a new scale-resolving turbulence model to supersonic retropropulsion flows with chemistry

Gabriel C. Nastac

APPLICATION OF A NEW SCALE-RESOLVING TURBULENCE MODEL TO SUPERSONIC RETROPROPULSION FLOWS WITH CHEMISTRY

Gabriel C. Nastac

A DISSERTATION

Submitted in partial fulfillment of the requirements
for the degree of Doctor of Philosophy
in
The Department of Mechanical and Aerospace Engineering
to
The Graduate School
of
The University of Alabama in Huntsville

May 2024

Approved by:

Dr. Abdelkader Frendi, Research Advisor/Committee Chair
Dr. Chang-kwon Kang, Committee Member
Dr. Sarma Rani, Committee Member
Dr. Gabriel Xu, Committee Member
Dr. Sivaguru S. Ravindran, Committee Member
Dr. George Nelson, Department Chair
Dr. Shankar Mahalingam, College Dean
Dr. Jon Hakkila, Graduate Dean

Abstract

APPLICATION OF A NEW SCALE-RESOLVING TURBULENCE MODEL TO SUPERSONIC RETROPROPULSION FLOWS WITH CHEMISTRY

Gabriel C. Nastac

A dissertation submitted in partial fulfillment of the requirements for the degree of Doctor of Philosophy

Mechanical and Aerospace Engineering

The University of Alabama in Huntsville

May 2024

Turbulent compressible flows are ubiquitous in many engineering applications of flight and propulsion. Computational fluid dynamics simulations are commonly performed to analyze these flows. Scale-resolving turbulence models inherently better capture various flow phenomena, including separation and mixing, as well as enable predictions of fluctuations, which can be critical for design compared to traditional steady-state turbulence models. In this work, new scale-resolving blended Partially-Averaged Navier-Stokes (BPANS) turbulence models are developed to account for compressibility effects and are employed to efficiently simulate turbulent compressible flows. Specifically, supersonic retropropulsion flows are investigated. Supersonic retropropulsion is a key technology for next-generation rockets. The new BPANS models are tested on a canonical supersonic mixing layer and experimental retropropulsion configurations. The model is also applied on a Mars lander retropropulsion concept to investigate gas model effects, including finite-rate chemistry to account for afterburning. Results from all these simulations are in good agreement with available experimental data.

Acknowledgements

First, I would like to express sincere thanks to my advisor Dr. Abdelkader Frendi for his continuous support and guidance during my PhD program. I am grateful to him for providing me the opportunity to contribute towards computational fluid dynamics research. I would also like to thank my PhD committee members, Dr. Chang-kwon Kang, Dr. Sarma Rani, Dr. Gabriel Xu, and Dr. Sivaguru Ravindran for their feedback and support in this work. Thanks to the University of Alabama in Huntsville for their academic and administrative support. Lastly, I would like to thank my family, friends, and loved ones for their unwavering encouragement and support over the years, without whom this work would not have been possible.

Table of Contents

List of Figures

List of Tables

List of Symbols

Symbol	Description
0	quantity at total conditions
A	Arrhenius factor, also matrix
C	specific heat
C_D	drag coefficient
C_T	thrust coefficient
C_p	pressure coefficient
D	diffusivity, also diameter
E	total energy
E_a	activation energy
F	blending function
H	height
I	identity matrix
J	diffusive flux, also jet
K	equilibrium constant
L	length
M	Mach number, also molecular weight

Symbol	Description
N_s	number of reactions
N_s	number of species
P	production
R	gas constant, also reaction rate, residual, or radius
Re	Reynolds number
S	strain rate tensor, also source term
T	temperature
V	volume
Δ	grid spacing, also difference
Ω	collision integral, also vorticity magnitude
α	angle of attack, also reactant stoichiometric coefficient
β	Arrhenius temperature exponent, also product stoichiometric coefficient and turbulence model coefficient
χ	ratio of turbulence variable to kinematic viscosity
δ	Kronecker delta
$\dot{\omega}$	chemical source term
$\dot{q}$	heat flux
γ	specific heat ratio, also turbulence model coefficient

Symbol	Description
∞	quantity at freestream conditions
κ	thermal conductivity, also von Kármán constant
$\mathrm{Pr_t}$	turbulent Prandtl number
$\mathrm{Sc_t}$	turbulent Schmidt number
μ	mixture dynamic viscosity
ν	mixture kinematic viscosity
ω	specific turbulent dissipation
$\overline{(\cdot)}$	Reynolds-averaged
ρ	mixture density
σ	turbulence model coefficient
τ	shear-stress tensor, also non-dimensional time
ε	turbulent dissipation
$\widetilde{(\cdot)}$	Favre-averaged
$\widetilde{\nu}$	turbulence working variable
$^\circ$	degrees
a	speed of sound
b	backward
c	molar concentration

Symbol	Description
d	distance to the wall, also dilation
e	internal energy, also exit
f	frequency, also forward or ratio
h	enthalpy
i,j,s	indices
k	reaction rate coefficient, also turbulent kinetic energy or Boltzmann constant
m	mass
n	Arrhenius temperature exponent
p	pressure
q	state vector
r	reaction
s	species, also shock
t	time
u	Cartesian velocity component
x	Cartesian direction
y	mass fraction
CC	compressibility correction

Symbol	Description
eq	equation
ref	reference quantity
rot	rotational
SFS	subfilter scale
t	turbulent quantity
tr	translational
u	universal
w	quantity at wall

Chapter 1. Introduction

Compressible flows are ubiquitous in many engineering applications of flight and propulsion. Applications include, but are not limited to, commercial aircraft flying at transonic speeds using jet engines, launch vehicles accelerating to hypersonic orbital velocities using rocket engines, and entry vehicles into planetary atmospheres. Engineers commonly perform computational fluid dynamics (CFD) simulations to analyze and design these vehicles.

Many compressible flows are also turbulent in nature. Turbulent flow is inherently an unsteady chaotic phenomena. However, the dominant methodology to simulate turbulent flows is using steady-state turbulence models which compute mean quantities of interest. While these steady-state models remove the time-component of simulations leading to reduced computational cost, they do not accurately predict fluctuations. In addition, the turbulence models are generally developed for canonical low-speed flows and applied to high-speed flows over complicated geometries. Many steady-state turbulence models also predict massively separated flow poorly over complex geometries, such as commercial aircraft.

It is desirable to perform scale-resolving simulations to better predict flow phenomena such as separation and mixing as well as fluctuations which can be

key drivers for a vehicle. Effective utilization of next-generation high-performance computing (HPC) architectures is key to reducing time-to-solution which is increased substantially for time-accurate simulations. Engineers generally cannot wait weeks for simulation turn-around if the goal is to impact vehicle design.

In the following section, a brief historic overview of turbulence modeling is presented.

1.1 Turbulence Modeling

Various turbulence modeling strategies are commonly employed as turbulence closures for CFD and are shown in Figure 1.1. Computational cost increases with height and modeling decreases with height. The following sections detail the various turbulence modeling strategies.

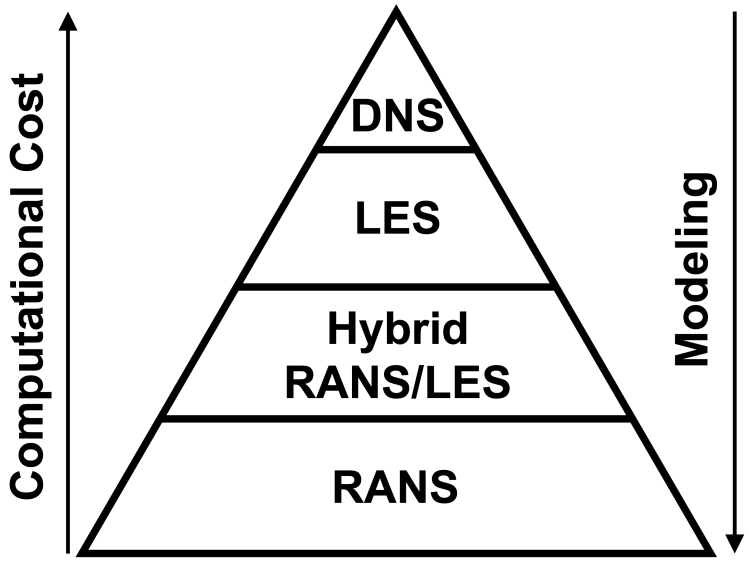

Figure 1.1: Turbulence modeling strategies.

1.1.1 Direct Numerical Simulation

If all the spatial and temporal scales are fully resolved, the Navier-Stokes governing equations can be solved without closures. This approach is denoted as direct numerical simulation (DNS). DNS is the most expensive method of simulation but also the most accurate as no models are necessary. The smallest eddies must be resolved which scale with Reynolds number. Reference [1] suggests the number of grid points needed for a DNS scales with Reynolds number to the 9/4 power. The authors estimate that for a small commercial aircraft cruising at transonic speeds, resolving just the turbulence near the surface requires roughly 10 quadrillion (10^{16}) grid points, which is many orders of magnitude larger than what simulations today employ. DNS is not currently feasible for most turbulent flows of interest for aerospace vehicles due to the high Reynolds numbers involved.

1.1.2 Reynolds-Averaged Navier-Stokes

On the other side of modeling (the base of the triangle) lie Reynolds-Averaged Navier-Stokes, commonly known as RANS, models. Using Reynolds decomposition, variables are split into mean and fluctuating components. Substituting the decomposition into the Navier-Stokes equations lead to various terms containing fluctuating components that require closures. Ultimately, RANS models do not resolve temporal turbulent fluctuations and instead model the turbulence. Steady state RANS models are widely used today for engineering and the primary methodology for turbulent flow simulations.

Two-equation RANS models originated in the early 1970s. The two primary models are $k-\varepsilon$ [2] and $k-\omega$ models [3]. These models start from the turbulent kinetic energy (TKE) transport equation which is derived using the momentum equations from Navier-Stokes and using Reynolds-Averaged or Favre-Averaged variables. Various terms require closures. For example, turbulent kinetic energy diffusion is closed using the Boussinesq approximation which is also employed in the Navier-Stokes equations for the Reynolds stresses. The production and destruction of TKE must also be closed through modeling. The TKE dissipation, denoted by ε typically, is solved using a similar transport equation. The $k-\varepsilon$ model was originally developed for shear layers and has reduced accuracy for flows with large pressure gradients. $k-\omega$ models have improved accuracy for wall-bounded flows and are also more stable. The turbulent dissipation, ε, and specific turbulent dissipation, ω, are linked with the following relation: $\omega = \varepsilon/(\beta^* k)$, where β^* is a model constant. Menter proposed a blended model [4] that combines these two models where both are advantageous, $k-\omega$ near walls and $k-\varepsilon$ away from walls.

Another more recent popular turbulence model is the Spalart-Allmaras (SA) model [5] developed in the early 1990s which is widely used for aerospace applications due to its accuracy, simplicity, and robustness. This model was developed primarily for external aerodynamics and wall-bounded flows. The SA model solves one transport equation for the turbulence field variable $\widetilde{\nu}$ which has units of kinematic viscosity. Compressibility corrections have been incorporated by Catris and Aupoix [6] to improve high Mach number skin friction and boundary

layer profile predictions which recover the logarithmic law of the wall. The SA model has also been extended to support hybrid turbulence model approaches described later in this chapter.

1.1.3 Large-eddy Simulation

Large-eddy simulation (LES) was proposed by Smagorinsky to model the weather in the early 1960s [7]. As the name implies, LES resolves only the large scale turbulent eddies which contain the majority of the total turbulent kinetic energy. Subgrid models are generally used to model unresolved scales which are more universal in nature. A low-pass filter is applied to the transport variables. Typically, the filter for LES is implicit and simply the grid size, although explicitly filtered LES [8] is possible and has been demonstrated for Cartesian grids.

Determining the quality of LES is still an active research topic [9]. One common approach is Pope's criterion [10] which is the ratio of subgrid turbulent kinetic energy over the total turbulent kinetic energy which is the sum of the resolved turbulent kinetic energy and the subgrid turbulent kinetic energy. When this quantity is below 20%, the simulation is assumed to be well-resolved. Evaluating the subgrid turbulent kinetic energy requires approximations as there are no explicit closures for the term. Another common approach to assess quality is the ratio of turbulent viscosity to molecular viscosity. In the limit of grid refinement, this ratio tends to zero. However, most LES models utilize an explicit filter, Δ. In theory, this filter should disappear when $\Delta \to \Delta_{DNS}$. Once again, determining what Δ_{DNS} is *a priori* generally is not possible. A previous study [11]

investigated the dynamic content in LES and DNS using Lyapunov exponents. The study showed in the limit of DNS, the global Lyapunov exponent saturates. The same problem occurs with this metric, in that determining this Lyapunov exponent is *a priori* not possible.

Even with these challenges in quantifying LES accuracy, LES has been successfully employed for various applications in various fields. The computational cost, however, is still large and requires high performance computing resources with large wall-times. LES is not currently feasible for most high Reynolds number turbulent flows of interest for aerospace vehicles. For example, for a transonic commercial aircraft, a wall-resolved LES is estimated to require on the order of a trillion grid points [12], which, while much lower than DNS requirements, is still not practically feasible today.

1.1.4 Hybrid RANS/LES

Hybrid RANS/LES models combine LES and RANS approaches. These include, but are not limited to, detached-eddy simulation (DES) [13], wall-modeled LES (WMLES) [14], unsteady RANS (URANS), and Partially-Averaged Navier-Stokes (PANS) [15, 16].

DES and WMLES are conceptually similar. Both use RANS models for the boundary layer portion of the flow field. DES models the full RANS equations using a full boundary layer grid in the actual simulation whereas WMLES solves the 1D wall-normal RANS equations using a virtual boundary layer grid for wall flux closure. DES models still have open problems such as modeled stress deple-

tion which can lead to grid-induced separation and smooth transition between RANS and DES zones [17]. Wall models are developed for attached turbulent flows and their use in flows with separation are also open research problems. One issue that affects both DES and WMLES models is that as the grid is refined, DNS is not recovered. DES by construction will be RANS in the boundary layer. WMLES models also have y^+ requirements to be valid. Another problem with wall models is that they do not accurately predict laminar flow regimes which are important and present in high-speed flows.

Another hybrid RANS/LES approach is URANS which involves simulating a RANS model with unsteady time stepping. URANS approaches generally are unable to resolve the small scales of turbulent flows and only capture the largest scale flow behaviors [18]. Many URANS simulations generally become steady state due to the large turbulent viscosity present in most turbulent flows.

1.1.5 PANS

PANS [15, 16] is another hybrid RANS/LES approach that enables bridging URANS to DNS in a more fundamental fashion. One issue with URANS and DES approaches is that in the limit of very fine grid resolution, the equations do not simplify to DNS. PANS methods adjust various components in the RANS equations using unresolved-to-total ratios of turbulent kinetic energy and dissipation. When these ratios are unity, PANS equations become the RANS equations. As these ratios tend to zero, the original Navier-Stokes equations are recovered and you have DNS. The variation of turbulence modeling is smooth between these

two limits. Using constant parameters enables distinction between numerical and modeling errors. Grid convergence is thus possible in the limit of fine grid.

There are still closures necessary for PANS. In theory, these resolution ratios are variable both in space and time for a given simulation as numerical error is never zero for realistic problems of interest. It is not possible to generally compute these variables *a priori*, especially for compressible flows typically encountered in aerospace. In practice, these ratios are constant throughout the flow field. While some closures do exist which can be used to estimate these ratios from an initial RANS simulation [19], they rely on incompressible homogeneous isotropic flow assumptions which are not valid for all flow configurations. In addition, some of these estimates are not bounded between 0 and 1 which introduces additional ambiguity [19]. Another approximation commonly employed for high Reynolds number flows which is used for this work is that the dissipation scales are not resolved at all, thus leading to a dissipation ratio, f_ε, of unity [16]. The only control parameter is thus the ratio of underresolved-to-total turbulent kinetic energy, f_k. Various PANS methods exist in literature including $k-\varepsilon$ [2] and $k-\omega$ [3] PANS models.

Recently, [20] proposed a Menter blended model [4] of the $k-\varepsilon$ and $k-\omega$ PANS models. Similar to RANS, $k-\omega$ PANS has near-wall benefits and $k-\varepsilon$ PANS has farfield benefits. This model, henceforth blended PANS or BPANS, is the key model extended and employed for this work. Chapter two covers the mathematical formulation of the model.

1.2 Contributions

The following work contributes to the state of the art in the following ways.

1.2.1 Extension of BPANS to High-speed Flows

The blended PANS (BPANS) model [20] has been implemented and extended to support compressible reacting high-speed flows in this work. The model has been implemented in compressible conservative form inside of a thermochemical nonequilibrium unstructured grid CFD solver [21]. In this implementation, the turbulent kinetic energy is fully coupled to the flow equations through the total energy equation. In addition, a compressibility correction has been incorporated to improve shear flow prediction. Most RANS models were originally developed for incompressible flows. The compressibility corrected BPANS model (BPANS CC) is capable of matching supersonic mixing layer mixing curves and growth rates versus the baseline BPANS model.

1.2.2 Investigation of an Air Retropropulsion Unit Problem with Various Turbulence Models Including the BPANS CC Turbulence Model

Supersonic retropropulsion (SRP) flows are important for various entry, descent, and landing (EDL) applications. Human-scale Mars atmospheric entry missions require an order of magnitude increase in payload capability compared to past robotic missions [22]. As payloads become larger, conventional deceleration

technologies such as parachutes become infeasible, necessitating alternate EDL strategies such as SRP. SRP is a key technology for re-usable rockets and proposed Human-scale Mars lander concepts [23].

There have been several experiments in past decades investigating supersonic retropropulsion (SRP) flows. Most experiments however, due to the physical constraints of simulating realistic rocket engines at wind tunnel scale, primarily utilize perfect gases [23]. There is a general gap in the understanding of the effects of chemistry and Martian conditions for these flows. Exhausting combustion products into the shock layer increases heat transfer for the liquid oxygen and methane engines planned for human Mars missions. During the powered descent phase, these human-scale landers travel through the atmosphere as well as the engine exhaust, so understanding the exhaust gas is vital to design and fly these next-generation vehicles. In addition, experiments have shown oscillatory and unstable flow behaviors; an understanding of these phenomena is necessary to reliably predict these flows for vehicle stability and control.

Figure 1.2 [21] depicts a characteristic flow field for SRP. A rocket engine plume expands out in front of a vehicle culminating into a terminal Mach disk. The Mach disk is a normal shock with incoming Mach numbers commonly over 10, leading to significant property variations over a small thickness. In addition, plume shear layers interact with the bow shock leading to a highly dynamic flow field with significant turbulence. Past experiments and simulations have shown that aerodynamic loads are not entirely insignificant and thus are important for

vehicle design. Ultimately, unsteady load prediction is required to determine the necessary control authority of vehicles employing SRP.

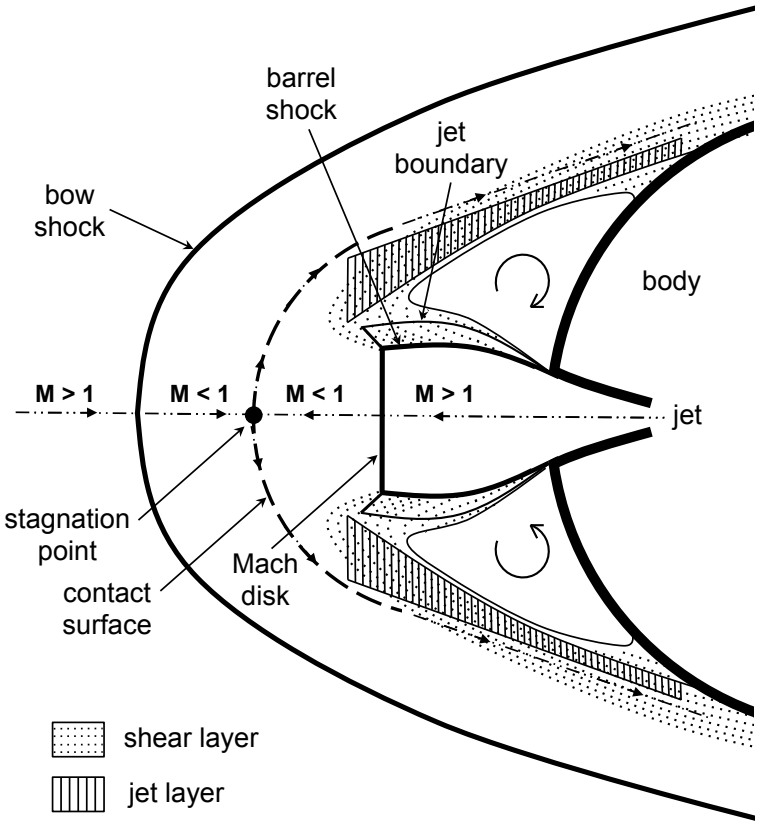

Figure 1.2: Characteristic flow field for supersonic retropropulsion.

While in reality, eventual SRP applications will involve high enthalpy chemically reacting flow, experimental limitations and complexities have led to an experimental focus on low temperature perfect gas experiments to capture the general flow field behaviors. There have been numerous experiments exploring perfect gas SRP flows with corresponding simulations. The primary simulation methodology during the last decade for SRP flows has been perfect gas

steady-state CFD simulations [23]. For example, Reference [24] simulates air experiments using the NASA OVERFLOW, DPLR, and FUN3D flow solvers using perfect gas assumptions and steady-state, 3-D RANS with reasonable agreement to each other and with the experimental data. Continuing work in Reference [25] simulated more recent experiments [26] using unsteady methods, including DES and URANS using the same three flow solvers with generally favorable agreement to the experiments. Reference [27] numerically investigated the effects of SRP on recent inert gas experiments done at the University of Virginia at hypersonic freestream Mach numbers using axisymmetric steady-state simulations. There are three main limitations in this study [27]: the freestream enthalpy levels are approximately two orders of magnitude smaller than Mars atmospheric entry; chemistry is neglected (both in the thrusters and in the atmosphere); and turbulence is neglected. Reference [28] investigated the effects of chemistry on capsule reaction control systems (RCS) using axisymmetric and semisymmetric 3-D steady-state simulations. Reference [29] simulated an SRP descent of the Falcon 9 using four CFD solvers, including FUN3D, using RANS with frozen and perfect gas species, a common methodology to simulate these flows. In general, the CFD solvers predict total forces and moments that favorably match the available flight data across most of the trajectory investigated. Reference [30] also simulated an SRP descent of a launch vehicle using the DLR TAU flow solver. One simulation in their matrix used finite-rate chemistry, with the rest being two perfect gas species RANS simulations. The one finite-rate chemistry simulation predicted a temperature increase of roughly 1000 K around the vehicle

base. Later simulations by the same group [31] investigated a similar setup using Spalart-Allmaras DES (SA DES) [13] with the two perfect gas species approach. Researchers at NASA [32] simulated a human-scale Mars lander concept based on upcoming perfect gas air experiments [33]. FUN3D was used to simulate the lander concept on the GPU-based Summit supercomputer [34], a U.S. Department of Energy resource located at the Oak Ridge Leadership Computing Facility [32]. Solution ensembles were performed to investigate the effects of spatial resolution, freestream Mach number, and engine throttle settings on the vehicle's resulting aerodynamics. Spatial domains were large enough to be measured in units of kilometers, and flow features on the scale of centimeters were resolved in the simulations. Pre-test simulations of a human-scale Mars lander concept have also been investigated using URANS and DES approaches [35, 36] based on upcoming perfect gas air experiments [33].

The newly developed BPANS turbulence model in this work was employed in simulating a canonical retropropulsion unit problem previously tested in a wind tunnel. This work is detailed in Reference [21]. The study investigated RANS as well as DES approaches. The RANS simulations were inadequate due to failing to capture unsteady flow phenomena and underpredicted surface pressures on the vehicle forebody. The unsteady models better captured surface pressures and predicted unsteady flow over the vehicle. The BPANS and BPANS CC models compared favorably to experimental and DES model results. The BPANS models better predicted surface pressure at various conditions and dominant frequencies versus the compressibility corrected DES approach.

1.2.3 Investigation of a Retropropulsion Unit Problem at Martian Conditions with Various Gas Models

Physically realistic CFD simulations of SRP flows require modeling scale-resolving turbulence and chemistry and are computationally expensive. Chemically reacting SRP flows are currently modeled using primarily 2-D, axisymmetric, and 3-D steady-state simulations. Current practice is to use two pseudo gas species, with one species representing the engine exhaust products and another representing the freestream or atmosphere, neglecting post-chamber reactions. These practices are in large part due to impractical computational time and cost. For design and analyses of these flows and vehicles, hundreds of simulations must be run. As such, efforts must be pursued to reduce time-to-solution for these complex flows, specifically in the area of high-fidelity CFD on emerging supercomputing architectures. A NASA group recently simulated a Mars lander concept with a chemical mechanism scaled to Martian conditions [37]. Experimental wind tunnel data for the air configuration are still in progress. The study compared the reacting flow simulations to perfect gas air simulations using dynamic similarity for many, but not all key parameters. The study also did not consider various gas models to determine the specific impact of chemistry.

It is ultimately desirable to use a pseudo species approach for aerodynamics to reduce computational cost. It is also desirable to use a computationally efficient turbulence model; LES is not feasible for these flows at this time. For accurate

prediction of time-accurate forces and moments, hybrid RANS/LES models must be employed. This work extends and applies the BPANS model to these flows.

As described above, it is effectively impossible to test Martian retropropulsion conditions on Earth and in wind tunnels and thus simulations are essential to improve our understanding of vehicle behavior and to reduce uncertainties. The previous experimental air configuration is re-utilized as a unit problem for a gas model investigation. A freestream Martian condition is tested which is representative of a re-entry condition. Various gas models were tested including: air, perfect gas CO_2, two pseudo-species (one representing engine exhaust and another the Martian freestream), and a 10-species mechanism with and without chemical reactions (reacting and inert). The newly developed BPANS CC model, shown to be predict similar or better results versus DES in the air study, is used for all the gas model simulations. This study serves as a benchmark problem for vehicle designers who commonly employ the various gas models used.

1.2.4 Extension of BPANS to GPUs

The BPANS model was developed in a hierarchical parallel way to enable efficient usage of GPUs which are vital to the next-generation HPC environment. The implementation builds upon previous work which is detailed in [38, 39]. The simulations in this work were performed primarily on GPUs, commonly a single node of a few GPUs. For example, the unsteady 10-species chemically reacting flow simulations were performed over night on a single GPU node with 8 GPUs.

To achieve the same turn-around, thousands of CPU cores would be necessary which require more power and space.

1.3 Overview

The following dissertation is organized as follows. Chapter two details the mathematical models used in the work. Chapter three details the numerical methods, and implementation used for the CFD simulations. Chapter four contains the simulation results. Initial verification and validation of the approach on canonical low-speed turbulent flows is presented. The work published in Reference [21] which include simulations and analysis of a canonical high-speed supersonic mixing layer simulation and a canonical air retropropulsion experiment using the newly developed BPANS model is also presented. The work in Reference [40] on the investigation of a unit retropropulsion problem using various gas models in a Martian environment is also detailed. Lastly, chapter five includes concluding remarks and future work.

Chapter 2. Mathematical Models

2.1 Compressible Reacting Flow Equations

The governing equations for turbulent compressible reacting flow are the Favre-Averaged Navier-Stokes equations which include the conservation of species, mixture momentum, and total energy

$$\frac{\partial}{\partial t}\left(\bar{\rho}\widetilde{y}_s\right) + \frac{\partial}{\partial x_j}\left(\bar{\rho}\widetilde{y}_s\widetilde{u}_j\right) - \frac{\partial}{\partial x_j}(\overline{J_{sj}}) = \widetilde{\dot{\omega}}_s, \tag{2.1}$$

$$\frac{\partial}{\partial t}\left(\bar{\rho}\widetilde{u}_i\right) + \frac{\partial}{\partial x_j}\left(\bar{\rho}\widetilde{u}_i\widetilde{u}_j + \bar{p}\delta_{ij}\right) - \frac{\partial}{\partial x_j}\left(\overline{\tau_{ij}}\right) = 0, \tag{2.2}$$

$$\frac{\partial}{\partial t}\left(\bar{\rho}\widetilde{E}\right) + \frac{\partial}{\partial x_j}\left(\left(\bar{\rho}\widetilde{E} + \bar{p}\right)\widetilde{u}_j\right) - \frac{\partial}{\partial x_j}\left(\widetilde{u_k}\overline{\tau_{kj}} + \overline{\dot{q}_j} + \sum_{s=1}^{N_s}\widetilde{h}_s\overline{J_{sj}} + \mu_k\frac{\partial k}{\partial x_j}\right) = 0, \tag{2.3}$$

where Reynolds-averaged and Favre-averaged variables are denoted by $\overline{(\cdot)}$ and $\widetilde{(\cdot)}$, respectively. $\widetilde{y}_s$ is the mass fraction of species s, $\bar{\rho} = \sum_{s=1}^{N_s}\bar{\rho}\widetilde{y}_s$ is the mixture density, $\widetilde{\rho}_s = \bar{\rho}\widetilde{y}_s$ is the species density of species s, $\widetilde{u}_i$ is the ith component of the velocity, and $\widetilde{E}$ is the total energy. $\overline{J_{sj}}$ is the jth component of the diffusive flux, $\widetilde{\dot{\omega}}_s$ is the chemical source term of species s, $\bar{p}$ is the pressure, $\overline{\tau_{ij}}$ is the shear-stress

tensor, $\overline{\dot{q}_j}$ is the jth component of the heat flux, $\widetilde{h}_s$ is the enthalpy of species s, and $\mu_k = (\widetilde{\mu} + \sigma_k \mu_t)$ is turbulent kinetic energy diffusion coefficient.

Constitutive relations for pressure, energy, enthalpy, the shear-stress tensor, diffusive flux, heat transfer, and the chemical source term are required to close the equation set. The gas is assumed to be an ideal gas; the pressure is thus defined as

$$\bar{p} = \sum_{s=1}^{N_s} \bar{\rho} \widetilde{y}_s \frac{R_u}{M_s} \widetilde{T} = \sum_{s=1}^{N_s} \bar{\rho} \widetilde{y}_s R_s \widetilde{T}, \tag{2.4}$$

where $\widetilde{T}$ is the temperature, R_u is the universal gas constant, and M_s and R_s are the molecular weight and gas constant of species s, respectively.

The turbulent kinetic energy k is defined as:

$$k = \frac{1}{2} \widetilde{u_i'' u_i''}. \tag{2.5}$$

The total energy $\widetilde{E}$ is defined as

$$\widetilde{E} = \frac{1}{2} \widetilde{u}_i \widetilde{u}_i + \sum_{s=1}^{N_s} \widetilde{y}_s \widetilde{e}_s + k, \tag{2.6}$$

where $\widetilde{e}_s$ is the internal energy of species s. For low-speed flows, generally $k << \widetilde{E}$ and the turbulent kinetic energy incorporation can be neglected. However, for high-speed flows, k can be a substantial portion of $\widetilde{E}$ and thus must be incorporated explicitly [41]. The total energy formulation in this work includes incorporation of k in the total energy, incorporation of molecular and turbulent k

diffusion in the total energy equation, and incorporation of k in the turbulent shear stress.

The internal energy is assumed to have fully excited rotational and translational modes and is defined as

$$\widetilde{e_s} = \int_{T_{\text{ref}}}^{\widetilde{T}} C_v^s dT + \widetilde{e}_{s,o}, \tag{2.7}$$

where C_v^s is the specific heat of species s at constant volume, T_{ref} is the reference temperature, and $\widetilde{e_{s,o}}$ is the energy of formation of species s at the reference temperature. The total enthalpy is $\widetilde{H} = \widetilde{E} + \bar{p}/\bar{\rho}$. In a similar fashion, species enthalpy $\widetilde{h_s}$ is defined as

$$\widetilde{h_s} = \int_{T_{\text{ref}}}^{\widetilde{T}} C_p^s dT + \widetilde{h_{s,o}}, \tag{2.8}$$

where $C_p^s = C_v^s + R_u/M_s$ is the specific heat of species s at constant pressure and $\widetilde{h_{s,o}} = \widetilde{e_{s,o}} + R_u T_{\text{ref}}/M_s$ is the enthalpy of formation of species s. NASA polynomials [42] are used to compute these properties on a per-species basis.

Viscous transport is closed with a Newtonian model with turbulence modeled using the Boussinesq eddy viscosity assumption [43]

$$\overline{\tau_{ij}} = 2\left(\widetilde{\mu} + \mu_t\right)\overline{S_{ij}} - \frac{2}{3}\bar{\rho}k\delta_{ij}, \tag{2.9}$$

where $\widetilde{\mu}$ is the dynamic viscosity, μ_t is the turbulent eddy viscosity computed by a turbulence model, and $\overline{S_{ij}}$ is the strain rate tensor computed as

$$\overline{S_{ij}} = \frac{1}{2}\left(\frac{\partial \widetilde{u}_i}{\partial x_j} + \frac{\partial \widetilde{u}_j}{\partial x_i}\right) - \frac{1}{3}\frac{\partial \widetilde{u}_k}{\partial x_k}\delta_{ij}. \tag{2.10}$$

Diffusive transport is closed with Fick's law

$$\overline{J_{sj}} = \bar{\rho}\left(\widetilde{D_s} + D_t\right)\frac{\partial \widetilde{y}_s}{\partial x_j}, \tag{2.11}$$

where $\widetilde{D_s}$ is the diffusivity of species s and $D_t = \mu_t/(\bar{\rho}\mathrm{Sc_t})$ is the turbulent diffusivity, where $\mathrm{Sc_t}$ is the turbulent Schmidt number, which is assumed constant.

Heat transfer is closed with Fourier's law

$$\overline{\dot{q}_j} = \left(\widetilde{\kappa} + \kappa_t\right)\frac{\partial \widetilde{T}}{\partial x_j}, \tag{2.12}$$

where $\widetilde{\kappa}$ is the thermal conductivity and $\kappa_t = C_p\mu_t/\mathrm{Pr_t}$ is the turbulent contribution to thermal conductivity, where $\mathrm{Pr_t}$ is the turbulent Prandtl number, which is assumed constant.

The chemical source term of species s per unit volume is defined as

$$\widetilde{\dot{\omega}}_s = M_s \sum_{r=1}^{N_r} \left(\beta_{s,r} - \alpha_{s,r}\right)\left(R_{f,r} - R_{b,r}\right), \tag{2.13}$$

where N_s is the number of reactions, $\alpha_{s,r}$ and $\beta_{s,r}$ are the stoichiometric coefficients for reactants and products in the reaction r, and $R_{f,r}$ and $R_{b,r}$ are the forward

and backward reaction rates defined as

$$R_{f,r} = 1000 \left[k_{f,r} \prod_{s=1}^{N_s} \left(0.001 \bar{\rho} \widetilde{y}_s / M_s\right)^{\alpha_{s,r}} \right], \tag{2.14}$$

$$R_{b,r} = 1000 \left[k_{b,r} \prod_{s=1}^{N_s} \left(0.001 \bar{\rho} \widetilde{y}_s / M_s\right)^{\beta_{s,r}} \right], \tag{2.15}$$

where $k_{f,r}$ and $k_{b,r}$ are the forward and backward reaction rate coefficients. The factors are present to convert between commonly used CGS units in reaction rate literature and SI units. The forward reaction rates are closed with the Arrhenius equation with three coefficients

$$k_f = A \widetilde{T}^{\beta} \exp\left[-\frac{E_a}{R_u \widetilde{T}} \right], \tag{2.16}$$

where A is the preexponential factor, β is a temperature exponent, and E_a is the activation energy for the reaction. The backward reaction rate is computed from the equilibrium constant, K, which is computed using Gibbs free energy and fit versus temperature

$$\frac{k_f(\widetilde{T})}{k_b(\widetilde{T})} = K(\widetilde{T}). \tag{2.17}$$

The transport properties (diffusivity, viscosity, and thermal conductivity) are computed using collision integrals [44]. The collision integrals, $\log_{10}\left(\pi \bar{\Omega}^{1,1}_{sr}\right)$ and $\log_{10}\left(\pi \bar{\Omega}^{2,2}_{sr}\right)$, are evaluated as curve fits versus temperature. The collision

integrals are modified as follows

$$\Delta_{sr}^{(1)} = \frac{8}{3}\sqrt{\frac{2M_sM_r}{\pi R_u T(M_s+M_r)}}\pi\bar{\Omega}_{sr}^{1,1}, \tag{2.18}$$

$$\Delta_{sr}^{(2)} = \frac{16}{5}\sqrt{\frac{2M_sM_r}{\pi R_u T(M_s+M_r)}}\pi\bar{\Omega}_{sr}^{2,2}. \tag{2.19}$$

The dynamic viscosity of the mixture is computed as

$$\widetilde{\mu} = \sum_{s=1}^{N_s} \frac{m_s \widetilde{c_s}}{\sum_{r=1}^{N_s} \widetilde{c_r}\Delta_{sr}^{(2)}}, \tag{2.20}$$

where $\widetilde{c_s} = \widetilde{y_s}/M_s$ is the molar concentration of species s and m_s is the mass of species s, per particle. The thermal conductivity is computed as the summation of translational and rotational components:

$$\widetilde{\kappa} = \widetilde{\kappa}_{tr} + \widetilde{\kappa}_{rot}. \tag{2.21}$$

The translational component is computed as

$$\widetilde{\kappa}_{tr} = \frac{15}{4}k\sum_{s=1}^{N_s} \frac{\widetilde{c_s}}{\sum_{r=1}^{N_s} a_{sr}\widetilde{c_r}\Delta_{sr}^{(2)}}, \tag{2.22}$$

where k is the Boltzmann constant and a_{sr} is defined as

$$a_{sr} = 1 + \frac{\left(1-(m_s/m_r)\right)\left(0.45-2.54(m_s/m_r)\right)}{\left(1+(m_s/m_r)\right)^2}. \tag{2.23}$$

Rotational contributions of the molecules of the mixture are computed as

$$\widetilde{\kappa}_{rot} = k \sum_{molecules} \frac{\widetilde{c}_s}{\sum_{s=1}^{N_s} \widetilde{c}_r \Delta_{sr}^{(1)}}. \tag{2.24}$$

Lastly, the diffusion is closed using binary diffusion. The binary diffusion for a pair of particles is defined as:

$$\widetilde{D}_{sr} = \frac{k\widetilde{T}}{\bar{p}\Delta_{sr}^{(1)}}. \tag{2.25}$$

The diffusion coefficient of species s is finally computed as:

$$\widetilde{D_s} = \frac{\widetilde{c}^2 M_s (1 - M_s \widetilde{c_s})}{\sum_{s=1}^{N_s} \widetilde{c_s} / \widetilde{D}_{sr}}, \tag{2.26}$$

where $\widetilde{c}$ is the mixture concentration

$$\widetilde{c} = \sum_{s=1}^{N_s} \widetilde{c_s}. \tag{2.27}$$

2.2 BPANS and BPANS CC Turbulence Models

The following section details the compressibility corrected Favre-averaged blended PANS model [20], based on the Menter Baseline (BSL) $k-\omega$ model [4]. The blended PANS model is also referred to as BPANS and BPANS CC with the compressibility correction. The governing equations follow closely to the original $k-\omega$ model [3]. There are two transport equations, one for the TKE (k) and another for the turbulent specific dissipation (ω). The model recovers the

original PANS $k-\omega$ near the wall in the boundary layer, and the $k-\varepsilon$ model away from the wall, through a blending function, enabling each model to be used in an effective manner. The transport equations fundamentally include five main terms: temporal derivative, convection, diffusion, production, and destruction. The governing equations are as follows:

$$\frac{\partial}{\partial t}\left(\bar{\rho}k\right)+\frac{\partial}{\partial x_j}\left(\bar{\rho}k\widetilde{u}_j\right)-\frac{\partial}{\partial x_j}\left(\left(\widetilde{\mu}+\sigma_k\mu_t\right)\frac{\partial k}{\partial x_j}\right)=S_k, \tag{2.28}$$

$$\frac{\partial}{\partial t}\left(\bar{\rho}\omega\right)+\frac{\partial}{\partial x_j}\left(\bar{\rho}\omega\widetilde{u}_j\right)-\frac{\partial}{\partial x_j}\left(\left(\widetilde{\mu}+\sigma_\omega\mu_t\right)\frac{\partial \omega}{\partial x_j}\right)=S_\omega. \tag{2.29}$$

The sources on the right hand side are given as:

$$S_k=\min\left(\mathcal{P},20\beta^*\bar{\rho}\omega k\right)-\beta^*\bar{\rho}\omega k+S_k^{CC}, \tag{2.30}$$

$$S_\omega=\bar{\rho}\gamma/\mu_t-\beta\bar{\rho}\omega^2+2(1-F_1)\frac{\bar{\rho}\sigma_{\omega 2}}{\omega}\frac{\partial k}{\partial x_j}\frac{\partial \omega}{\partial x_j}+S_\omega^{CC}, \tag{2.31}$$

which include the blending function F_1 which blends the two models. The production of TKE is computed as

$$\mathcal{P}=\overline{\tau_{ij}^{SFS}}\frac{\partial \widetilde{u}_i}{\partial \widetilde{x}_j}, \tag{2.32}$$

$$\overline{\tau_{ij}^{SFS}}=2\mu_t\overline{S_{ij}}-\frac{2}{3}\bar{\rho}k\delta_{ij}, \tag{2.33}$$

where the turbulent viscosity, μ_t is computed using the transport variables and density: $\mu_t=\frac{\bar{\rho}k}{\omega}$. SFS denotes subfilter scale; for RANS, the SFS stress reduces to the Reynolds stress.

The blending function F_1 is computed as

$$F_1 = \tanh\left(arg_1^4\right), \tag{2.34}$$

$$arg_1 = \min\left[\max\left(\frac{\sqrt{k}}{\beta^* \omega d}, \frac{500\widetilde{\mu}}{\bar{\rho} d^2 \omega}\right), \frac{4\bar{\rho}\sigma_{\omega 2} k}{CD_{k\omega} d^2}\right], \tag{2.35}$$

$$CD_{k\omega} = \max\left(2\bar{\rho}\sigma_{\omega 2}\frac{1}{\omega}\frac{\partial k}{\partial x_j}\frac{\partial \omega}{\partial x_j}, 10^{-20}\right). \tag{2.36}$$

The various constants above are also blended with the blending function, with constants denoted by 1 and 2 subscript:

$$\phi = F_1\phi_1 + (1 - F_1)\phi_2. \tag{2.37}$$

The remaining constants to close the model are presented in Table 2.1. The PANS extensions through the underresolved-to-total ratios of TKE f_k and dissipation f_ε are included appropriately.

2.2.1 Compressibility Correction

The mixing-layer growth rate decreases with increasing Mach number [41]. Most popular turbulence models (*e.g.*, SA, $k-\varepsilon$, $k-\omega$, and other variants) over-predict this mixing-layer growth rate in compressible regimes and instead predict the incompressible growth rate (which increases with increasing Mach number) which they are empirically fit for.

Various compressibility corrections (CC) were developed in the 1980s and 1990s to better model the compressibility effects in high-speed mixing layers.

Table 2.1: Values of BPANS turbulence model constants.

Constant	Value
β^*	0.09
κ	0.41
σ_2^*	$\frac{1}{1.3}\frac{f_\varepsilon}{f_k^2}$
γ_1	$\frac{5}{9}$
γ_2	0.42
$\sigma_{\omega 1}$	$2.0\frac{f_k^2}{f_\varepsilon}$
$\sigma_{\omega 2}$	$1.3\frac{f_k^2}{f_\varepsilon}$
σ_{k1}	$2.0\frac{f_k^2}{f_\varepsilon}$
σ_{k2}	$\frac{f_k^2}{f_\varepsilon}$
β_1	$0.05\left(1-\frac{f_k}{f_\varepsilon}\right)+0.075\frac{f_k}{f_\varepsilon}$
β_2	$0.0378+\frac{f_k}{f_\varepsilon}0.045$

The corrections involve empirical functions of the turbulent Mach number that are calibrated to match experimental data and available DNS. Most of these developed mixing layer compressibility corrections unfortunately negatively affect high-speed wall-bounded flows [45] by under-predicting skin friction and heat transfer. Most RANS models do well at predicting high-speed (up to Mach 5) attached boundary layer flows without any corrections; compressibility effects are presumed to be small in boundary layers [45]. It is thus desirable to apply the shear layer compressibility correction only away from the wall.

The specific CC used in this work is the one detailed by Suzen and Hoffmann in [46] which builds upon the Sarkar model [41]. The model is fit to match experimental and DNS turbulent compressible mixing data. Two additional sources are added to the total dissipation: an additional dissipation due to compressibility effects, and an additional term to incorporate additional dissipation due to pressure dilatation. Using the $k-\varepsilon$ model, the new terms are:

$$\varepsilon_C = \alpha_1 \bar{\rho} \varepsilon M_t^2, \tag{2.38}$$

$$\overline{p'd''} = \overline{p' \frac{\partial u_j''}{\partial x_j}} = -\alpha_2 \bar{\rho} P_k M_t^2 + \alpha_3 \bar{\rho} \varepsilon M_t^2, \tag{2.39}$$

where P_k is the production of the TKE equation. All the terms include a turbulent Mach squared dependence due to experimental data available. For PANS, no additional adjustments are necessary; all the terms match the general dissipation of TKE which is unchanged for PANS formulations. Transforming these source terms to $k-\omega$ models ($\varepsilon = \beta^* k\omega$) and applying $k-\varepsilon$ / $k-\omega$ blending yields:

$$S_k^{CC} = (1-F_1)\left(-\alpha_1 \bar{\rho} \beta^* k\omega M_t^2 + \overline{p'd''}\right), \tag{2.40}$$

$$S_\omega^{CC} = (1-F_1)\left(\alpha_1 \bar{\rho} \beta^* \omega^2 M_t^2 - \frac{\bar{\rho}}{\mu_t}\overline{p'd''}\right), \tag{2.41}$$

where the turbulent Mach number is $M_t = \sqrt{\frac{2k}{a^2}}$, where a is the local speed of sound. The correction is only applied away from the wall through the blending function F_1, which is beneficial once again as the corrections negatively impact wall-bounded portions of the flow. The pressure dilatation coefficients are fit by

Sarkar based on DNS data ($Re_\lambda \approx 25$) and the additional dissipation is fit on experimental data:

$$\alpha_1 = 1.0, \tag{2.42}$$

$$\alpha_2 = 0.4, \tag{2.43}$$

$$\alpha_3 = 0.2. \tag{2.44}$$

2.3 Spalart-Allmaras with Catris-Aupoix Corrections Turbulence Model

Turbulence is also modeled using the one-equation Spalart-Allmaras model [5] with Catris-Aupoix compressibility corrections [6] in this work. The primary differences of this model include accounting for density variations and retrieving the logarithmic law of the wall for high-speed flows. The one-equation model is given as:

$$\begin{aligned}\frac{\partial \bar{\rho}\tilde{\nu}}{\partial t} + \widetilde{u}_j \frac{\partial \bar{\rho}\tilde{\nu}}{\partial x_j} = c_{b1}(1 - f_{t2})\hat{S}\bar{\rho}\tilde{\nu} - \left[c_{w1} f_w - \frac{c_{b1}}{\kappa^2} f_{t2}\right] \bar{\rho} \left(\frac{\tilde{\nu}}{\hat{d}}\right)^2 + \\ \frac{1}{\sigma}\frac{\partial}{\partial x_j}\left(\widetilde{\mu}\frac{\partial \tilde{\nu}}{\partial x_j}\right) + \frac{1}{\sigma}\frac{\partial}{\partial x_j}\left(\sqrt{\bar{\rho}}\tilde{\nu}\frac{\partial \sqrt{\bar{\rho}}\tilde{\nu}}{\partial x_j}\right) + \frac{c_{b2}}{\sigma}\frac{\partial \sqrt{\bar{\rho}}\tilde{\nu}}{\partial x_i}\frac{\partial \sqrt{\bar{\rho}}\tilde{\nu}}{\partial x_i}.\end{aligned} \tag{2.45}$$

The turbulent eddy viscosity is computed identically to the original SA model as

$$\mu_t = \bar{\rho}\tilde{\nu} f_{v1}, \tag{2.46}$$

where

$$f_{v1} = \frac{\chi^3}{\chi^3 + c_{v1}^3}, \tag{2.47}$$

where $\chi = \tilde{\nu}/\widetilde{\nu}$ is the ratio of the turbulence variable $\tilde{\nu}$, and the molecular kinematic viscosity, $\widetilde{\nu} = \widetilde{\mu}/\bar{\rho}$. $\hat{S}$ is given by

$$\hat{S} = \Omega + \frac{\tilde{\nu}}{\kappa^2 \hat{d}^2} f_{v2}, \tag{2.48}$$

$$\hat{d} = \min(d, C_{DES} h_{max}), \tag{2.49}$$

where $\Omega = \sqrt{2W_{ij}W_{ij}}$ is the magnitude of the vorticity, and $\hat{d}$ is the minimum of the distance to the wall, d, and the maximum distance to an adjacent dual cell centroid, h_{max}, multiplied by C_{DES} for conventional DES [13]. Table 2.2 details the standard constants used, and the remaining functions are defined as

$$f_{v2} = 1 - \frac{\chi}{1 + \chi f_{v1}}, \tag{2.50}$$

$$f_w = g \left[\frac{1 + c_{w3}^6}{g^6 + c_{w3}^6} \right]^{1/6}, \tag{2.51}$$

$$g = r + c_{w2}(r^6 - r), \tag{2.52}$$

$$r = \min \left(\frac{\tilde{\nu}}{\hat{S} \kappa^2 \hat{d}^2}, 10 \right), \tag{2.53}$$

$$f_{t2} = c_{t3} \exp(-c_{t4}\chi^2), \tag{2.54}$$

$$c_{w1} = \frac{c_{b1}}{\kappa^2} + \frac{1 + c_{b2}}{\sigma}, \tag{2.55}$$

and

$$W_{ij} = \frac{1}{2}\left(\frac{\partial \widetilde{u}_i}{\partial x_j} - \frac{\partial \widetilde{u}_j}{\partial x_i}\right). \tag{2.56}$$

Table 2.2: Values of SA turbulence model constants.

Variable	Value
c_{b1}	0.1355
c_{b2}	0.622
σ	2/3
κ	0.41
c_{w2}	0.3
c_{w3}	2
c_{v1}	7.1
c_{t3}	1.2
c_{t4}	0.5
C_{DES}	0.65

Chapter 3. Method of Solution

3.1 Numerical Implementation

Due to the complex geometry of aerospace vehicles, unstructured grids are commonly employed for ease of gridding. Fully Unstructured Navier-Stokes 3D (FUN3D) is CFD software developed at the NASA Langley Research Center to simulate complex flows across the speed range [47] and is the software used in this work. The equations are solved with the method of lines (MOL). The spatial domain is discretized using a node-based finite-volume approach on general unstructured grids that can include tetrahedra, pyramids, prisms, and hexahedra. Node-based approaches are commonly used in other practical unstructured CFD solvers such as DLR TAU [48] and SU2 [49]. A median-dual volume is constructed around each node by connecting the edge midpoints with the face centers and the centroids of the primal elements. Figure 3.1 illustrates the dual and primal cell volumes in two dimensions. In 3D, the dual of a tetrahedral grid is a polyhedral grid with roughly 15 edge neighbors per node.

The inviscid fluxes are computed at edge medians using an approximate Riemann solver such as Roe's scheme [50] or HLLE++ [51]. Second-order accuracy is obtained using an unstructured Monotonic Upstream-centered Scheme for Conservation Laws (MUSCL) reconstruction [52] with unweighted least-squares

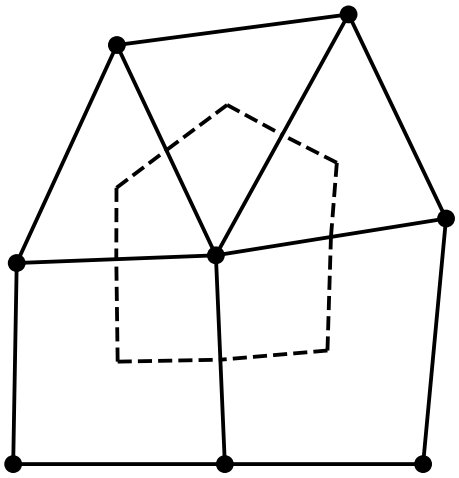

Figure 3.1: Grid nomenclature: Solid lines denote primal grid elements while dual volumes are denoted by dashed lines.

gradients computed at each node. The upwinding parameter, κ, which blends central and upwind reconstruction is set to 0.5 in this work. The van Albada flux limiter [53] is utilized for MUSCL. The inviscid fluxes and Jacobians are computed in loops over edges or dual-faces of the grid. The viscous fluxes are discretized using Green-Gauss element-based gradients. For tetrahedral grids, this is equivalent to a Galerkin-type approximation. On other element types, the edge-based gradients are combined with the Green-Gauss element-based gradients; this improves the stability of the viscous operator. The viscous fluxes and Jacobians are computed in loops over cells of the grid. In each cell, cell-averaged quantities are computed as well as cell-based gradients. Edges or dual-faces inside the element are then looped over to compute their corresponding half of the flux. Source terms and Jacobians are computed over nodes (dual-cells). Gradients for sources

are computed using Green-Gauss node-based gradients. For boundary conditions, fluxes are computed and added to the residual over boundary nodes. Dirichlet, or strong, boundary conditions are employed for most wall variables. Velocity is explicitly set to zero and temperature is specified for constant wall temperatures on wall boundary nodes. The turbulence variables also use Dirichlet boundary conditions and are set explicitly on the wall appropriately.

The equations are typically integrated in time using implicit formulations such as first-order backward Euler or second-order backward difference (BDF2) approximations to the time derivative, although explicit methods such as Strong-Stability-Preserving Runge-Kutta 3 stage (SSP-RK3) [54] are also available. BDF2 is the time-integration scheme used for this work. Generally, the time step restriction for high Reynolds number boundary layers necessitate implicit methods. Grids of complex geometry commonly have poor quality edges which further hamper the CFL number of explicit methods.

The conservation equations can be rewritten in vector form

$$\int_V \frac{\partial \mathbf{q}}{\partial t} dV + \oint_S (\mathbf{F} \cdot \mathbf{n})\, dS - \int_V \mathbf{S} dV = \mathbf{0}. \tag{3.1}$$

The total number of equations is $N_{eq} = 3 + N_s + N_e + N_t$, where three equations represent momentum conservation, N_s is the number of species, N_e is the number of energies (thermochemical equilibrium is assumed in this work, so there is just one energy equation) and N_t is the number of turbulence model equations (2 for BPANS, 1 for SA-Catris, or 0 for laminar/inviscid flows). The vector $\mathbf{q} = [\bar{\rho}\vec{\widetilde{y}_s}, \bar{\rho}\vec{\widetilde{u}}, \bar{\rho}\widetilde{E}, \bar{\rho}k, \bar{\rho}w]^T$ is the vector of conserved variables, $\mathbf{F} = \mathbf{F}_i - \mathbf{F}_v$ is the

$N_{eq} \times 3$ flux tensor, $\mathbf{F}_i$ is the inviscid flux tensor, $\mathbf{F}_v$ is the viscous flux tensor, and $\mathbf{S}$ is the source term vector. Integration is performed over the dual volumes.

The discrete nonlinear equations can be written in a compact form where time integration is taken as first-order backward Euler for simplicity

$$V\frac{\mathbf{q}^{n+1}-\mathbf{q}^{n}}{\Delta t}+\mathbf{R}(\mathbf{q}^{n+1})=\mathbf{0}. \tag{3.2}$$

Here, V is the dual volume, Δt is the physical time step, $\mathbf{q}^n$ is the vector of conserved variables defined at time step n, and $\mathbf{R}$ is the spatial residual vector. The system of nonlinear equations is solved using a defect correction method and pseudotime as

$$\left[\frac{V}{\Delta\tau}\mathbf{I}+\frac{V}{\Delta t}\mathbf{I}+\frac{\partial\hat{\mathbf{R}}}{\partial\mathbf{q}}\right]\Delta\mathbf{q}=-\mathbf{R}(\mathbf{q}^{n+1,m})-\frac{V}{\Delta t}\left(\mathbf{q}^{n+1,m}-\mathbf{q}^{n}\right), \tag{3.3}$$

$$\mathbf{q}^{n+1,m+1}=\mathbf{q}^{n+1,m}+\Delta\mathbf{q}. \tag{3.4}$$

Here, m is the implicit nonlinear iteration index, $\Delta\tau$ is the local pseudotime step, $\mathbf{I}$ is the identity matrix, and $\mathbf{q}^{n+1,1}=\mathbf{q}^{n}$. After completion of nonlinear iterations, the final solution at $n+1$ is denoted as $\mathbf{q}^{n+1}$. The approximate Jacobian $\partial\hat{\mathbf{R}}/\partial\mathbf{q}$ is based on a linearization of first-order inviscid fluxes and second-order viscous fluxes. The linearization is performed around the latest solution, $\mathbf{q}^{n+1,m}$, and involves only contributions from nearest neighbors. The Jacobian matrix is sparse and composed of $N_{eq} \times N_{eq}$ dense blocks. The matrix $\mathbf{A}=\left[\frac{V}{\Delta\tau}\mathbf{I}+\frac{V}{\Delta t}\mathbf{I}+\frac{\partial\hat{\mathbf{R}}}{\partial\mathbf{q}}\right]$ is segregated into diagonal and off-diagonal blocks. The

number of off-diagonal blocks in each row corresponds to the number of nearest neighbors and is typically between 15 (regular tetrahedral grids) and 26 (regular hexahedral grids).

A multicolor point-implicit approach is used to obtain approximate solutions of the linear system of equations at each nonlinear iteration. In this approach, the system of equations is colored such that no two adjacent unknowns are assigned the same color. Colors are processed sequentially. Since the matrix **A** is constructed using only nearest-neighbor relations, unknowns defined at the grid vertices of the same color do not depend on each other and can be updated in parallel in a Jacobi-like fashion. Unknowns within each color are further segregated into those comprising interior values and those required for partial halo exchanges with neighboring grid partitions in order to facilitate effective overlapping of communication and computation while recovering the serial algorithm. Finally, the entire system of equations is renumbered to achieve optimal use of memory bandwidth. Since the discrete nonlinear iterations are cast in update form, judicious use of mixed-precision arithmetic is leveraged to reduce memory traffic. The solver implementation was extensively optimized for a broad range of matrix block sizes in previous work and supports FP64, FP32, and FP16 arithmetic. For further details on the implementation, the following references include more information: [55] and [56].

3.2 GPU Implementation

Graphics processing units (GPUs) are specialized hardware chips that have over an order of magnitude larger concurrency than multicore central processing units (CPUs). GPUs have demonstrated accelerated computing for various applications ranging from traditional scientific simulations to deep learning [57] in the last decade. Of the current top ten supercomputers in the world listed on the current TOP500 [58], nine utilize GPUs (see Table 3.1). Of the top 100 supercomputers, over half utilize GPUs. This growth is expected to continue in the upcoming decade. In addition, U.S. exascale systems rely on Intel and AMD GPUs [59, 60, 61]. GPUs are significantly more power efficient than CPUs which is largely the reason for this usage. For example, if you simply multiplied the OLCF Jaguar system compromised of CPUs in 2009 to an exaflop, the power required would be over 3 GW. The current Frontier system requires less than 20 MW of power for an exaflop, which is over 150 $\times$ more efficient. Effective utilization of GPUs is key for next-generation aerospace vehicle design and analysis as noted in the NASA CFD vision 2030 study [62].

Many large-scale science applications are primarily memory bound including finite-volume CFD. Performance thus scales with memory bandwidth. A dual-socket CPU system has a memory bandwidth on the order of a few hundred GB/s. A single high-end GPU has memory bandwidths on the order of a few thousand GB/s, using similar power. In specifics, an AMD EPYC 7742 Dual-Socket CPU with 128 total cores has a specified memory bandwidth of 409.6 GB/s

at 450 watts power [63]. An NVIDIA H100-NVL GPU has a specified memory bandwidth of 7800 GB/s at 700 watts power [64]. The GPU is roughly 12 × more efficient in terms of memory bandwidth per watt which is directly correlated to performance for memory bound problems. A single NVIDIA H100-NVL GPU is similar to approximately 1500 AMD EPYC 7742 cores.

Table 3.1: Global HPC Landscape. Top 10 supercomputers.

Rank	Organization	System Name	CPU/GPU	Rmax (PF)	Year
1	ORNL	Frontier	GPU	1200	2022
2	ANL	Aurora	GPU	585	2023
3	Microsoft	Eagle	GPU	561	2023
4	RIKEN	Fugaku	CPU	442	2020
5	EuroHPC	LUMI	GPU	380	2020
6	EuroHPC	Leonardo	GPU	239	2020
7	ORNL	Summit	GPU	150	2018
8	EuroHPC	MareNostrum	GPU	138	2023
9	NVIDIA	SuperPOD	GPU	121	2023
10	LLNL	Sierra	GPU	95	2018

3.2.1 Programming Model

Due to the increased concurrency and throughput of modern GPUs, algorithms generally need to be adapted to expose more parallelism. In addition, unfortunately, it is not currently possible to simply compile previous CPU software and run on GPUs efficiently. With cloud computing at the forefront of modern day HPC, performance is important. Simply running on GPUs is not the target; if it is cheaper to run software on CPUs, then people will simply do that.

There are many various programming models that one can use to run on GPUs. One of the first programming paradigms is NVIDIA's Compute Unified Device Architecture (CUDA) [65], released in 2007. CUDA C++, henceforth CUDA, utilizes single instruction, multiple data (SIMD) execution and is thus optimal for computations that can be run concurrently on multiple data elements. Computations may be divided over thousands of threads, which are processed using streaming multiprocessors (SMs). The threads are organized into blocks, which are themselves organized into warps (currently 32 threads) that run on SMs.

One limitation of CUDA is that it is tied to NVIDIA hardware. In the recent decade, there have been various programming paradigms to program various hardware architectures. Directive-based approaches include OpenACC [66] and OpenMP [67]. Programming models besides CUDA include OpenCL [68], AMD Heterogeneous Interface for Portability (HIP) [69], and SYCL [70]. Abstractions above these various models have also been developed such as Kokkos [71] and

RAJA [72]. Ultimately, these models all rely and utilize a SIMD paradigm and are quite similar syntactically.

The CFD implementation in this work utilizes a thin abstraction layer above CUDA to enable efficient execution on NVIDIA GPUs (through CUDA), AMD GPUs (through HIP), and Intel GPUs (through SYCL) as well as traditional CPUs with a single code-base. The software syntax follows CUDA and uses C macros to preprocess the code at compile time to the other backends depending on the target architecture. At the core function level, the syntax is ultimately similar to the original Fortran implementation of the solver. References [38, 39] includes more details on the approach including implementation details and results. The software has been used at scale on thousands of NVIDIA and AMD GPUs on the OLCF Summit and Frontier systems [34, 60].

For multi-device, coarse-grained message passing interface (MPI) [73] with conventional domain decomposition is used. As a rule of thumb, for efficiency and saturation, each GPU should have a million grid points for perfect gas flows.

3.2.2 Design Approach

Due to Amdahl's law and the fact that the GPU memory bandwidth is much large than the typical PCIe bus to move data to and from the GPU, the entirety of the partial differential equations solve is performed on the GPUs. The only data transferred between the GPUs and CPUs are during pre-processing and post-processing. Integrated scalar quantities such as residual norms and forces and moments are the primary data copied back and forth during a single time

step. The CPU code in this case simply acts as a high level driver calling device functions asynchronously. To maintain backwards compatibility with the existing Fortran code, data structures remain identical including data layout which maintains column ordering. Precision is also maintained, with most of the solver using FP64 which is generally needed to maintain numerical accuracy in high Reynolds number boundary layer grid cells.

Several optimizations had to be performed which are detailed in Reference [38]. As there are thousands of concurrent threads, atomic operations are used to handle race conditions. In addition, algorithms had to increase parallelism to achieve optimal GPU performance. For example, in a Jacobian calculation, instead of a single thread computing a local Jacobian on an edge or node, many threads can concurrently compute it. An additional consideration is memory hierarchy. Memory speed increases with locality. Storage on a thread is significantly faster than main memory. However, each thread has limited memory, typically on the order of 100 FP64 values. By utilizing hierarchical parallelism, that is using many threads to compute a work item like a flux or Jacobian, more local thread memory is available to the algorithm to enable improved performance. State reduction is one of the most important optimization techniques for the chemically reacting CFD implementation. Lastly, thread divergence must also be minimized. The primary reason GPUs are efficient is that operations occur on multiple data at the same time. If threads do not perform the same algorithm, then much of the performance is lost as threads in a block must wait to synchronize with the slowest thread. Algorithms have been rewritten to minimize algorithm divergence.

With respect to the BPANS implementation, Jacobians for the turbulent contributions employ hierarchical parallelism. For the source term, there are contributions to the species that are considered in addition to the two turbulent transport variables. The turbulent kinetic energy incorporation to the total energy equation are also considered in the Jacobians.

Chapter 4. Results and Discussion

4.1 Low-Speed BPANS Validation

To validate the BPANS model for low-speed flows, previous incompressible backward-facing step and flow over a cylinder cases which were used in the incompressible BPANS validation [20] are simulated for comparison. The OpenFOAM [74] CFD solver was utilized in the previous work which is also a 2nd order finite-volume CFD solver. Overall, results match well quantitatively to the OpenFOAM implementation. The BPANS implementation also behaves as expected with varying ratios tested.

4.1.1 Wall-bounded Flows

A backward-facing step setup is considered to validate wall-bounded flows. This case examines reattachment of separated turbulent shear layers which are present in many aerodynamics flows of interest including airfoils, diffusers, and cavities. Large separation leads to reduced aerodynamic efficiency. Accurate prediction of separated flows is key for the design of these vehicles as separation drives key flow conditions such as take-off and landing of airplanes.

A backward-facing step geometry enables investigating the reattachment process independently as the flow will separate at the step location. The experi-

mental setup described in [20] is considered. The freestream velocity is 44.2 m/s at atmospheric total pressure and temperature. This flow condition corresponds to a freestream Mach number of approximately 0.13. The Reynolds number based on the step height is 37,500.

The computational domain is $10H \times 5H \times 3H$ upstream of the step and $20H \times 6H \times 3H$ downstream of the step. A hexahedral multi-block structured grid is generated and a side view of it is shown in Figure 4.1. The grid contains 2.6 million cells, with the span consisting of 60 cells. The grid has $y^+ < 1$ and $z^+ < 60$ for the first point off the wall for the domain. The streamwise resolution varies from $x^+ \approx 1$ to $x^+ \approx 140$ at 5H downstream. Following the reference and previous studies with comparable resolution f_k is set to 0.2 and f_ε is set to 0.667.

As the solver in this work is compressible and this is a very low Mach number flow, a low-dissipation Roe scheme developed for low Mach number flows [75] is employed rather than the standard Roe scheme [50] to reduce dissipation. Walls are treated as adiabatic and no-slip. Side walls are treated as periodic. The inlet is set to uniform freestream conditions. The outlet is set to a back pressure at slightly below atmospheric pressure. The same time step as the reference is utilized. The time step is set to 5 μs which is approximately 70 non-dimensional time steps per reference time based on the freestream velocity and step height. Statistics are averaged in time and across the span in space over 50 flow through times.

Isosurfaces of Q-criterion are plotted in Figure 4.2 to visualize flow structures. The turbulence caused by separation is clearly observed. Mean velocity

profiles at $x/H = 5$ from the step are plotted in Figure 4.3. Mean resolved turbulent kinetic energy profiles are plotted in Figure 4.4. Results agree reasonably well with previous simulations and experiments. The reattachment point is slightly under predicted compared to experiment.

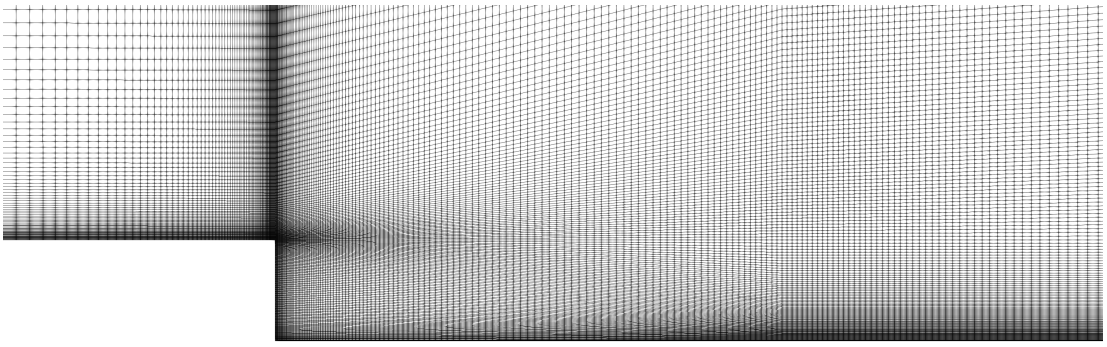

Figure 4.1: Backward step grid slice.

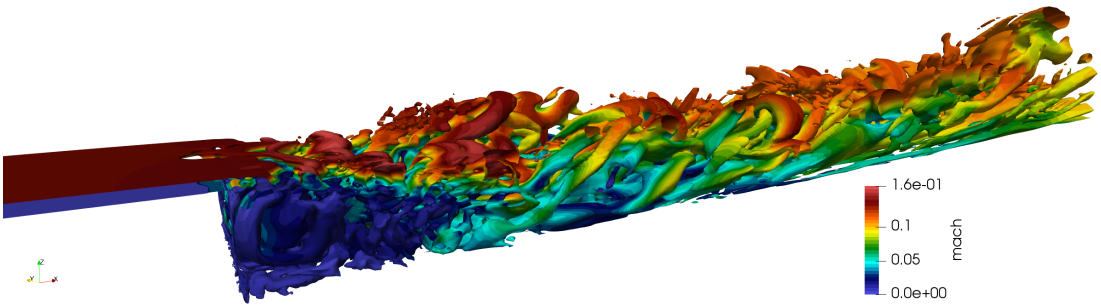

Figure 4.2: Backward step isosurfaces of non-dimensional Q-criterion (0.1) colored by Mach number.

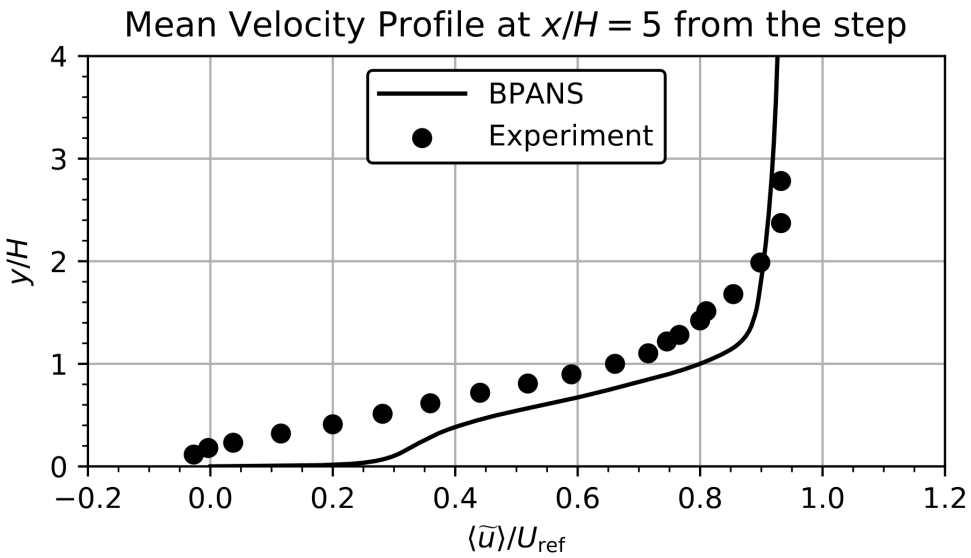

Figure 4.3: Backward step mean velocity profiles at $x/H = 5$ from the step.

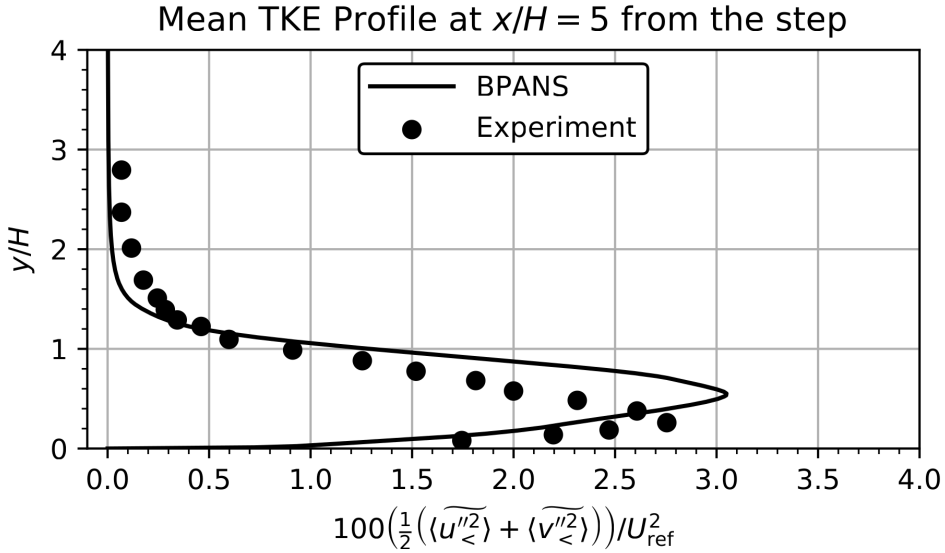

Figure 4.4: Backward step resolved turbulent kinetic energy profiles at $x/H = 5$ from the step.

4.1.2 Free-shear Flows

Free-shear behavior is also present in aerodynamic flows of interest, generally through wakes and engine exhaust. The flow behavior is primarily governed by turbulent mixing and less so by wall effects. The flow around a circular cylinder is considered which involves strong vortex shedding downstream. The experimental setup of [76] is specifically investigated. The Reynolds number based on the cylinder diameter is $Re_D = 1.4 \times 10^5$. The freestream velocity is 21 m/s, which corresponds to a freestream Mach number of 0.06. Similar to the previous study, the low-dissipation low Mach Roe scheme [75] is employed.

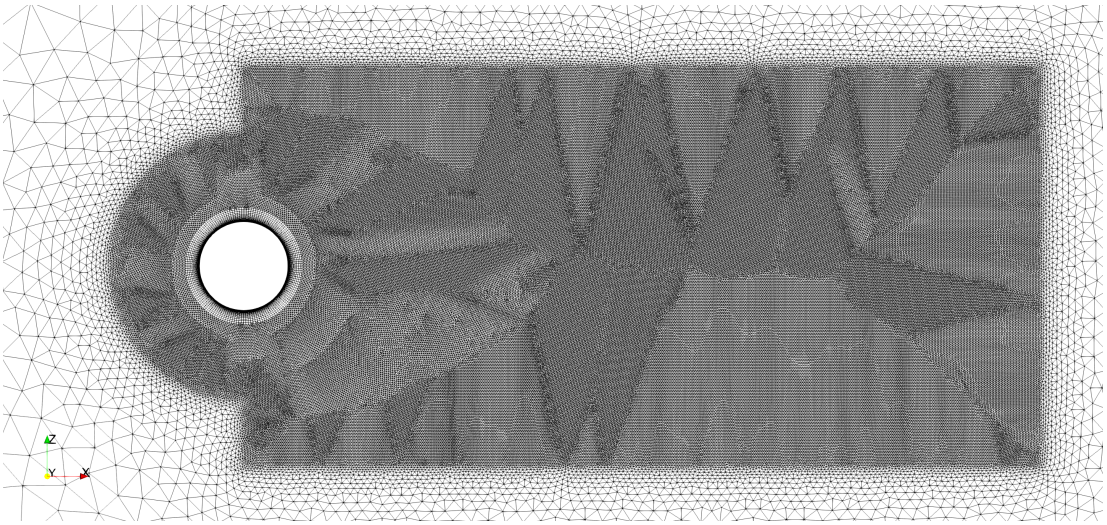

Figure 4.5: Cylinder grid slice.

The computational setup follows that of Reference [20]. A 2D unstructured grid is generated with a quad boundary layer near the cylinder and triangles in the wake, matching target spacing for the reference including a spacing of $y^+ = 1$

for the first point off the wall. The core of the wake has spacing 0.02D on the plane. The 2D grid is extruded to reach a span of three diameters with 50 cells across the span. In total the grid contains 6.2 million points or dual control volumes. A slice of the grid is shown in Figure 4.5. Walls are treated as adiabatic and no-slip. Side walls are treated as periodic. The time step is approximately 0.7 ms which is approximately 70 non-dimensional time steps per reference time based on the freestream velocity and cylinder diameter. Statistics are averaged in time and across the span in space over 100 flow through times denoted by a reference length of 10 diameters. An f_k of 0.5 is used and the underresolved-to-total turbulent kinetic energy dissipation is assumed to be unity following past simulations.

Overall results agree well with past simulations and experiments. Figure 4.6 plots isosurfaces of Q-criterion colored by Mach number showing the large coherent turbulent structures in the wake. The streamwise velocity along the axial centerline is shown in Figure 4.7. The streamwise velocity is slightly underpredicted near $x/D = 8$. The streamwise and vertical velocity versus z at $x/D = 1$ are plotted in Figures 4.8 and 4.9 with very good qualitative and quantitative agreement to experiment. The streamwise velocity is also plotted at $x/D = 3$ in Figure 4.10. The mean surface pressure around the cylinder is plotted in Figure 4.11. The separation point is overpredicted by about 5° versus experiment. Overall surface pressures agree well with experiment away from the separation point.

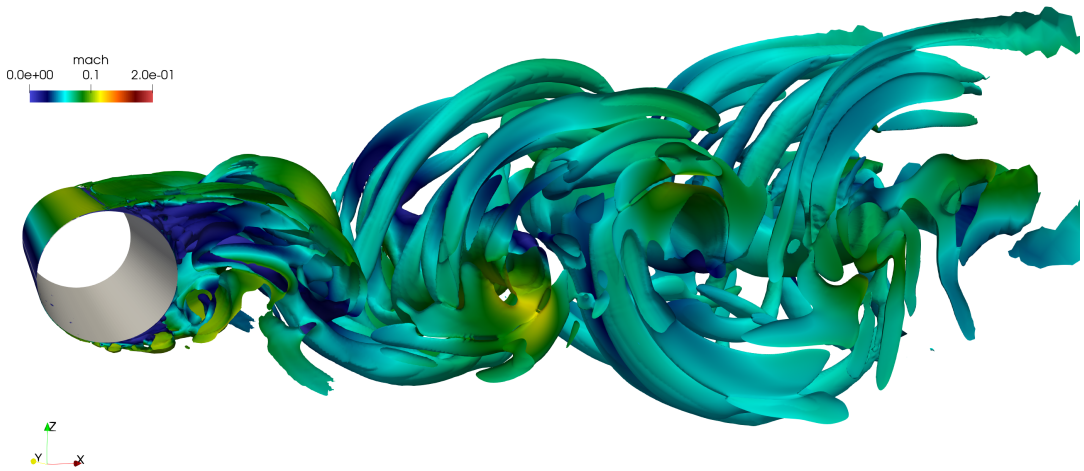

Figure 4.6: Cylinder flow isosurface of non-dimensional Q-criterion (0.001) colored by Mach number.

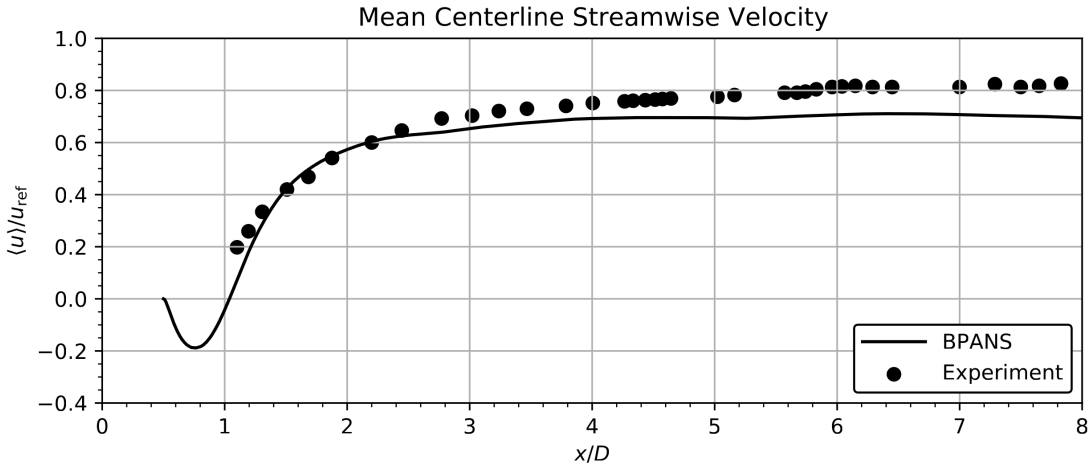

Figure 4.7: Cylinder flow mean centerline streamwise velocity profile.

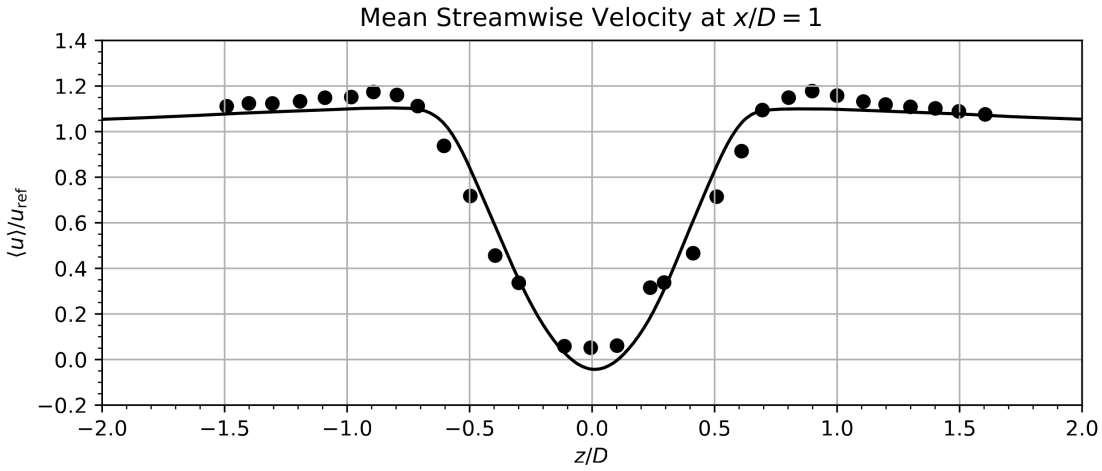

Figure 4.8: Cylinder flow mean streamwise velocity profile at $x/D = 1$.

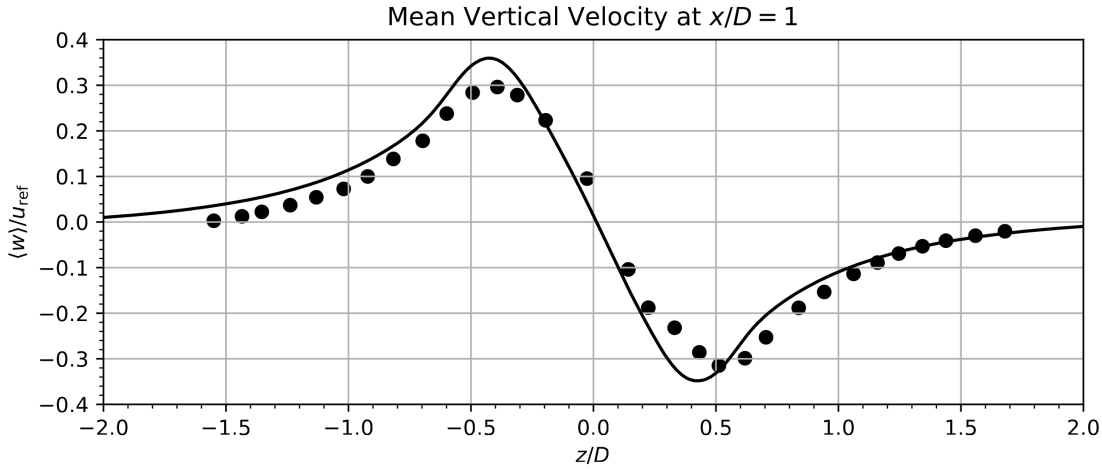

Figure 4.9: Cylinder flow mean vertical velocity profile at $x/D = 1$.

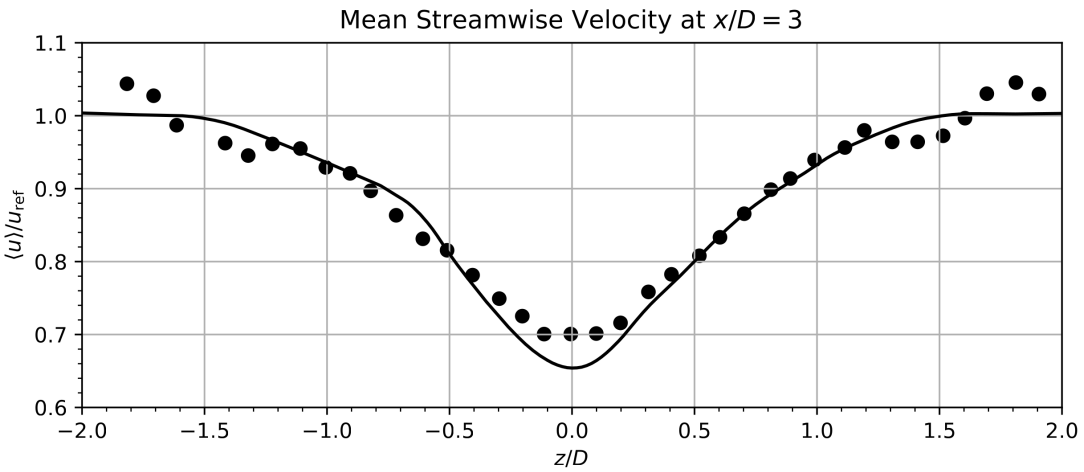

Figure 4.10: Cylinder flow mean streamwise velocity profile at $x/D = 3$.

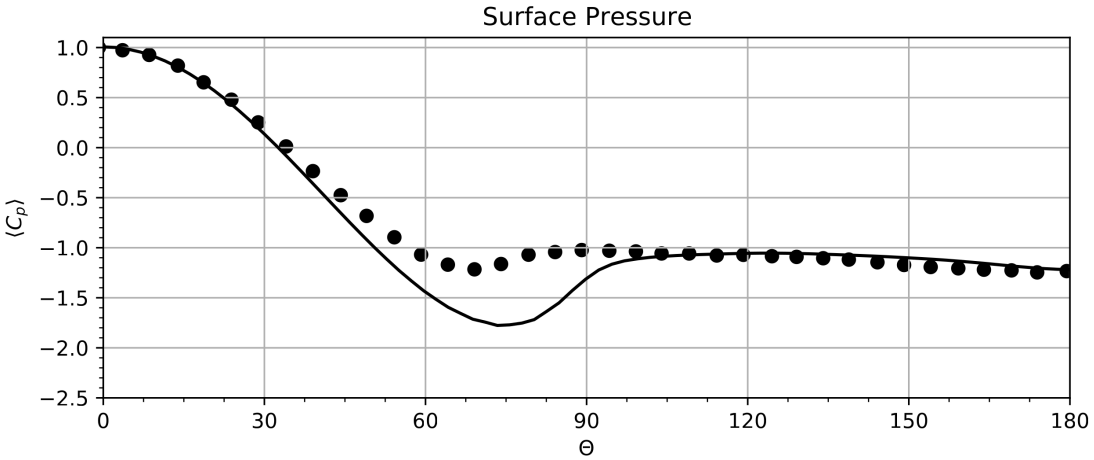

Figure 4.11: Cylinder flow mean surface pressure versus degrees around the cylinder. 0° corresponds to the stagnation point.

4.2 Supersonic Flows

The following section details the various supersonic flow cases investigated in this work. BPANS was previously shown to perform well in the incompressible regime for free shear flows. Free shear flows are also very common in the compressible regime. A well-known supersonic mixing layer is first considered to demonstrate BPANS and BPANS CC on a canonical supersonic flow and the results show good agreement with experimental data. The models are then employed on a complex perfect gas air supersonic retropropulsion configuration based on an experimental setup. Comparisons of BPANS and BPANS CC to URANS and DES methods as well as experimental data are performed. Good agreement between the simulations and experimental data are observed. The same retropropulsion configuration is then scaled to Martian conditions. Various gas modeling approaches are employed including pure CO_2, pseudo species, and a chemical mechanism to model the afterburning of the engine plumes in the Martian atmosphere. The scale-resolving CFD simulations are compared to simulation and experimental data of the air configuration. The lower fidelity gas modeling simulations are also compared against the higher fidelity chemical mechanism simulation to examine the impact of gas models on plume flow fields and forces and moments that are of interest to vehicle design.

4.2.1 Supersonic Mixing Layer

High-speed spatially developing shear layer simulations of the Goebel and Dutton experiment [77] have been carried out using BPANS. The specific condition investigated has a freestream Reynolds number based on the upper condition of about $Re_\infty = 30 \times 10^6\ 1/m$ and the two mixing stream Mach numbers are $M_1 = 2.01$ and $M_2 = 1.38$, respectively.

A 45 million cell hexahedral multi-block structured grid was generated for a domain of length 0.35 meters which includes the upstream splitter plate which is modeled with a length of 0.05 m. The splitter plate height is 500 microns. The simulation width is 0.01 m which is discretized into 32 uniform width cells. The walls are resolved and modeled with no-slip. The inflows are set to supersonic conditions corresponding to the experimental conditions. Extrapolation is utilized on the outflow plane. The two side planes are assumed periodic and the top and bottom domains are modeled as z-symmetry. The walls are meshed with a $y^+ = 1 \approx 1\ \mu$m based on the freestream Reynolds number and cells with x-y aspect ratio of 4 and O($y^+ \approx 100$) were generated in the bulk of the shear layer. The width spacing, z^+, is O($y^+ \approx 300$). The x-y aspect ratio of the cells at the plate lip is unity. The grid is shown in Figure 4.12.

The equations are integrated in time using a two-step backward difference (BDF2) scheme with a time step of 0.25 μs which corresponds to a global CFL of about 80 due to resolving the wall, and is of order unity in the shear layer away from the plate. Five subiterations are used which correspond to nominally 2 orders

of magnitude residual reduction for the equations. Once statistically stationary flow is achieved, statistics are obtained over 5 flow through times, where a flow through time is defined by the top plate freestream velocity and domain length.

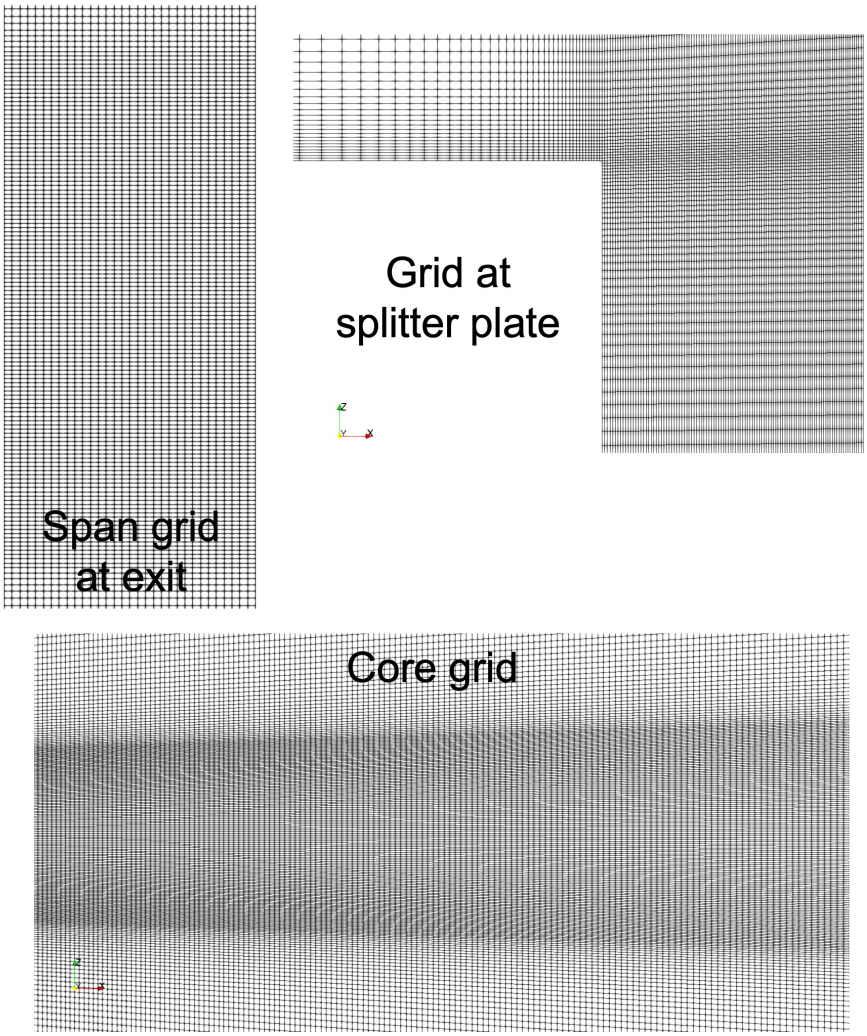

Figure 4.12: Mixing layer grid slices. Top left: span grid at exit. Top right: grid at top half of splitter plate. Bottom: grid in the core of the shear layer.

BPANS is run for f_k ratios of unity and 0.2, the latter implying the grid is resolving 80% of the turbulent kinetic energy. Compressibility corrections are

also tested for both ratios. The stream velocity similarity profile is shown in Figure 4.13. The mixing layer thickness, b, is defined as the transverse distance between mean streamwise velocities of $U_1 - 0.1\Delta U$ and $U_2 + 0.1\Delta U$. Results are found to be self-similar and free from lip shock effects starting from $x = 0.10$ m. The growth rate is obtained from $x = 0.10$ m and $x = 0.25$ m locations. Figure 4.14 depicts non-dimensional y-velocity (periodic direction) contours. Overall, all the models predict the similarity profile well. RANS results ($f_k = 1.0$) predict a sharper mixing layer curve near the tails than the BPANS ($f_k = 0.2$) results and the experimental data. The RANS results do not become unsteady and thus have no y-velocity components. Both BPANS approaches are unsteady and better predict the mixing layer curve versus the RANS results. For both ratios, the compressibility corrected models better predict the experimental growth rate (db/dx). The predicted growth rate error is reduced from 15% to less than 5% with the compressibility correction for this condition for both $f_k = 1.0$ and $f_k = 0.2$. The compressibility correction was developed for RANS initially, so agreement is expected for the $f_k = 1.0$ simulations. For the $f_k = 0.2$ simulations, the compressibility correction increases the growth rate due to increased mixing from more scales being resolved rather than modeled. Overall, the results indicate that BPANS CC can be used to successfully predict canonical supersonic compressible flows. The $f_k = 0.2$ results matching experimental mixing and growth rate demonstrate the capability to simulate unsteady flows which are increasingly becoming important for prediction of unsteady loads for vehicle design and analysis.

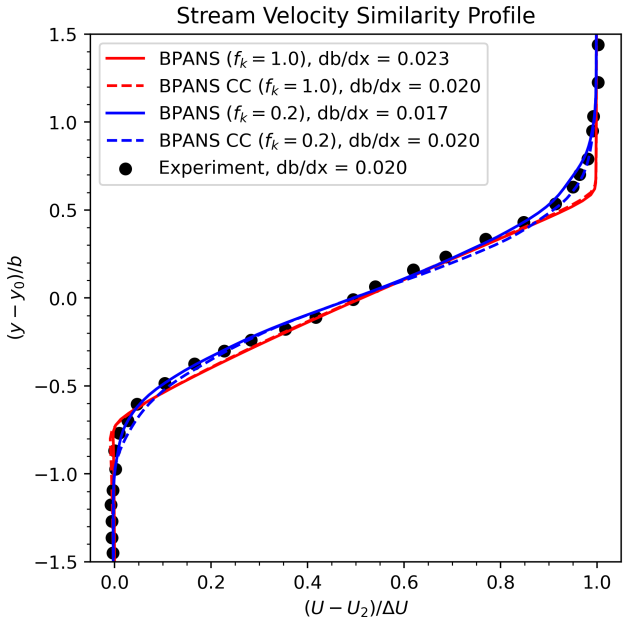

Figure 4.13: Mixing layer stream velocity similarity profile with comparison to experimental data.

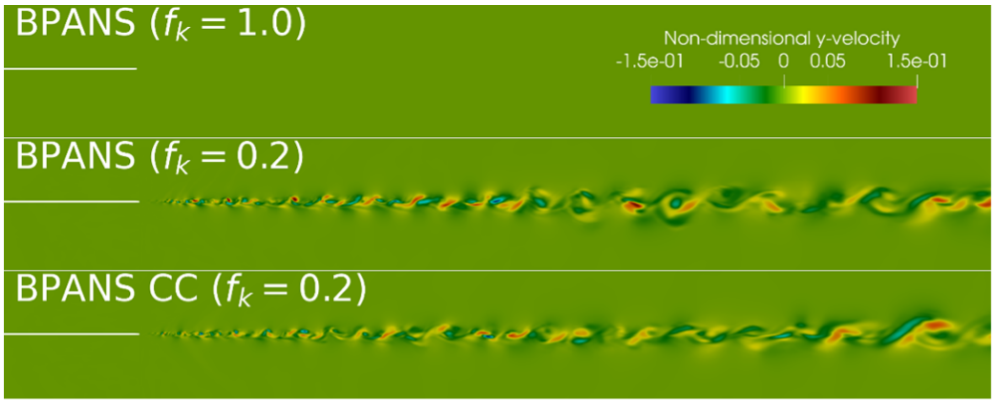

Figure 4.14: Mixing layer y-velocity contours at the y-centerline. The RANS results ($f_k = 1.0$) do not exhibit unsteadiness and thus have a y-velocity of zero. The velocity is nondimensionalized by the upper plate velocity.

4.2.2 Supersonic Retropropulsion Flows

A perfect gas SRP experimental configuration [26] is investigated with various turbulence modeling approaches. The freestream Mach number is 4.6 and the freestream Reynolds number per meter is 5 million. The heat shield is a 70-degree sphere cone with a diameter of 5 inches. The engine exit diameter, D_e, is 0.5 inches. The nozzle exit-to-throat area ratio is 4. The plenum total temperature and pressure are set according to the experimental setup as $p_0/p_\infty = 7724.3$ and $T_0/T_\infty = 5.34$. The freestream air is cold, and thus a perfect gas assumption is valid and used for these simulations.

Unstructured grids are utilized here due to the complexity of the geometry. A family of grids are generated with varying refinement. Figure 4.15 depicts the first grid consisting of 80 million cells and 15 million points. All walls are modeled as no slip adiabatic walls. A prismatic boundary layer with an initial wall spacing targeting a $y^+ = 1$ is generated, with the farfield grid composed of tetrahedra. There is an engine spacing source of $\Delta/D_e = 0.04$. A spherical source outside the nozzle exit and surface has a spacing of $\Delta/D_e = 0.15$. Farfield spacing is set to $\Delta/D_e = 0.4$. Two finer grids are generated by decreasing the surface and volume spacing sources by 25% and 50%, leading to grids approximately two and three times larger than the original grid. Steady state BPANS ($f_k = 1.0$), or RANS, simulations are performed on the three grids and results are presented in Figure 4.16. Grid convergence is obtained successfully, with the original 80 million cell grid being adequately resolved for surface property prediction.

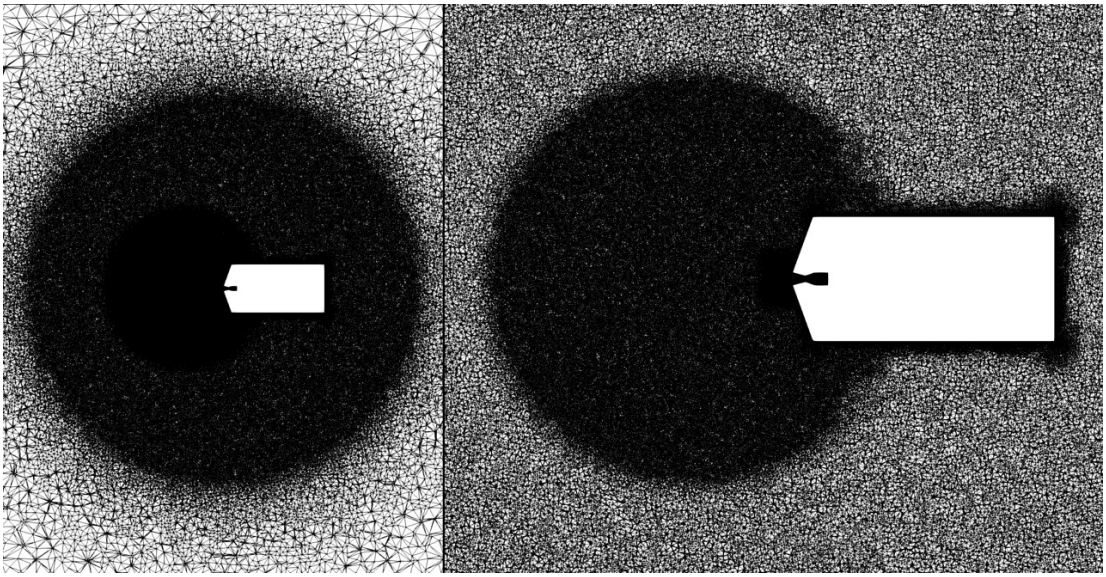

Figure 4.15: Y-plane centerline slice of 15 million point unstructured SRP grid.

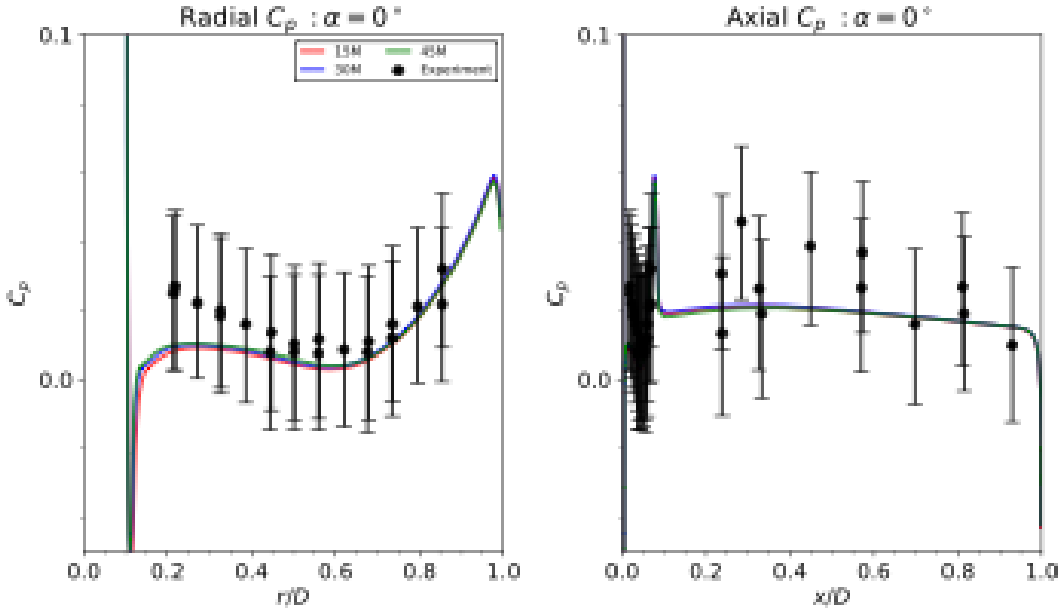

Figure 4.16: SRP grid convergence study using RANS.

BPANS, BPANS CC, and DES turbulence models are used for unsteady flow prediction. Equations are integrated in time with BDF2 with a time step of one microsecond. Three subiterations are used leading to nominally two orders of magnitude residual reduction. BPANS and BPANS CC with $f_k = 0.2$ are used. Three angles of attack are considered: $0°, 12°$, and $20°$. Simulations are time-averaged after quasi steady state is obtained for roughly 10 milliseconds, or about 20 periodic cycles for the $0°$ angle of attack configuration.

The nominal thrust coefficient, C_T, is 2.0, with all models predicting coefficients within 2% of nominal. For this example, the thrust is the dominant contribution to the total force; the maximum aerodynamic component is roughly 15% of the total. While aerodynamic contributions are not a significant component of the mean forces, aerodynamic fluctuations are fundamentally what drive what the vehicle guidance navigation and control system is required to provide for stability and control.

Figures 4.17-4.19 depicts pressure coefficient data. Mean pressure coefficients agree well with experimental data. The models predict unsteady flowfields which contrasts with the RANS approach (Figure 4.16) which did not have significant variance. BPANS with $f_k = 0.2$ better predicts pressure coefficient data compared to $f_k = 1.0$ (Figure 4.16), which emphasizes the improved prediction capabilities of unsteady hybrid RANS/LES models versus traditional RANS approaches. The BPANS CC model better predicts nose surface pressure for the $12°$ and $20°$ angle of attack cases. Along the axial part of the vehicle, the impact of

the compressibility correction is small since flow Mach numbers are much smaller versus the jet plume at the forebody.

Overall, BPANS CC with $f_k = 0.2$ and DES models compare very favorably. For the larger angle of attack, BPANS CC better predicts the surface pressure on the nose of the vehicle versus DES. Standard deviations are shown for the zero angle of attack configuration in Figure 4.20. Standard deviations are over predicted slightly but follow experimental trends for all the unsteady models. The largest discrepancy in standard deviation occurs at the mid radial point. The experiment considered random error, flowfield nonuniformity, and model/instrumentation asymmetries for the error bars, with most of the error due to flowfield nonuniformity. The simulations here neglect freestream turbulence fluctuations which can impact shock dynamics and ultimately surface property prediction. In addition, side walls are not modeled; side wall turbulence does exist for this facility which can be seen in numerical schlieren of the experiments. Aerodynamic drag for the three angles of attack are shown in Figures 4.21-4.23. The forces on the vehicle are nearly periodic for the zero angle of attack configuration and become more unsteady and ultimately chaotic for the higher angles of attack. The force frequencies decrease as angle of attack increases as well.

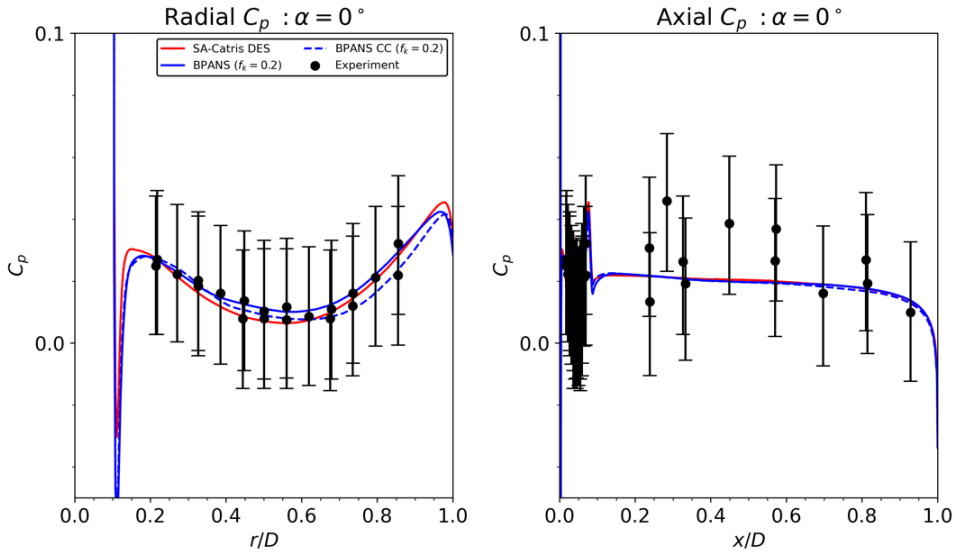

Figure 4.17: Surface pressure coefficient statistics for the SRP configuration at 0° angle of attack.

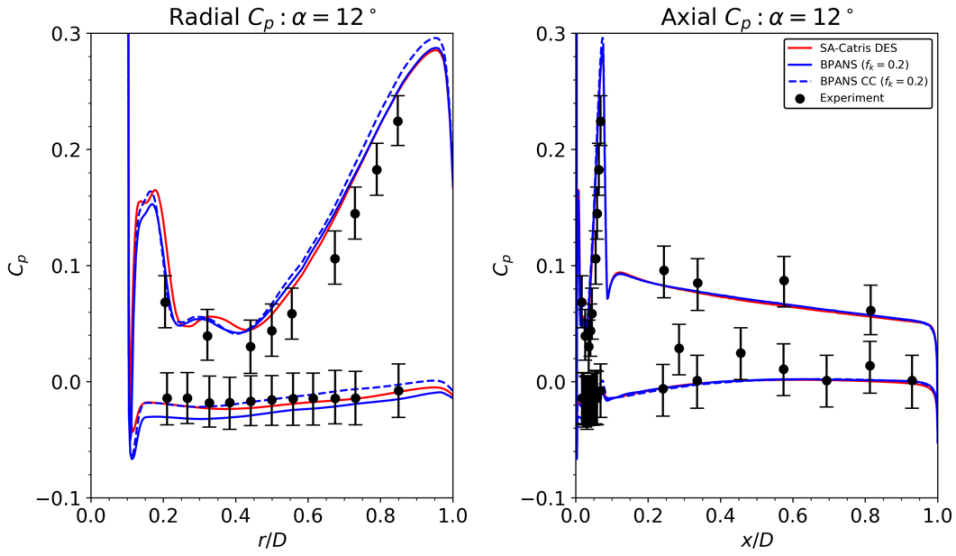

Figure 4.18: Surface pressure coefficient statistics for the SRP configuration at 12° angle of attack.

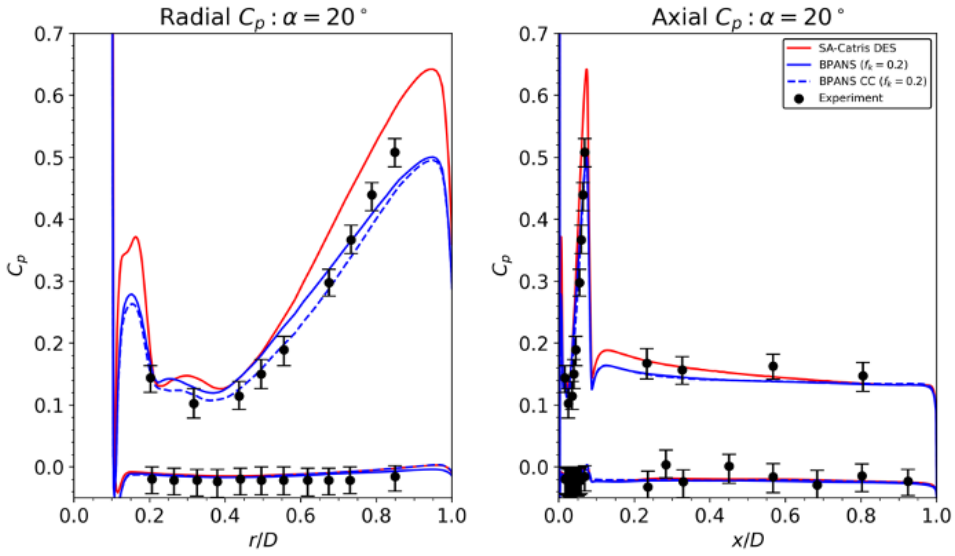

Figure 4.19: Surface pressure coefficient statistics for the SRP configuration at 20° angle of attack.

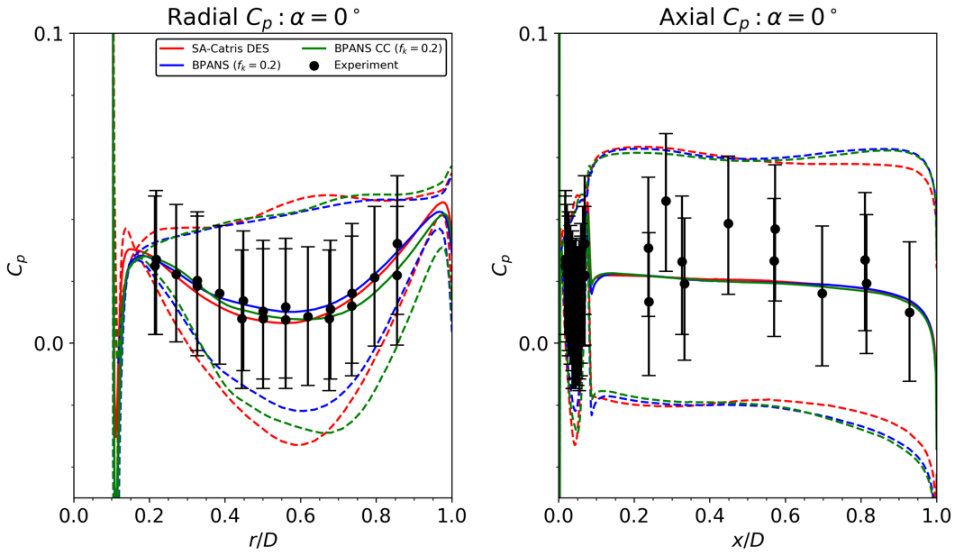

Figure 4.20: Surface pressure coefficient statistics with variance for the SRP configuration.

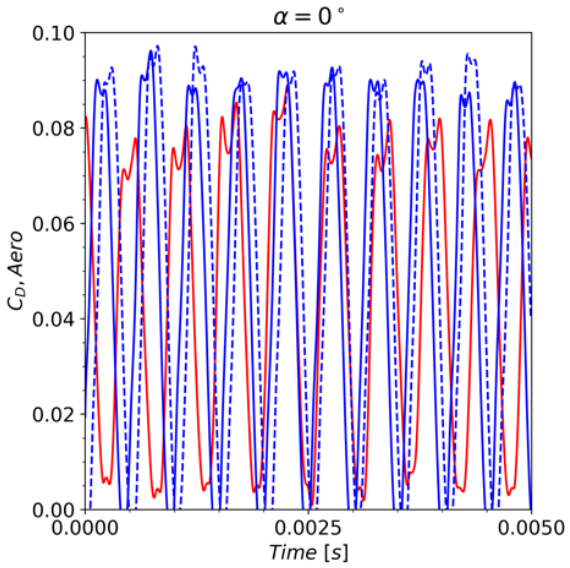

Figure 4.21: Aerodynamic drag versus time for 0° angle of attack.

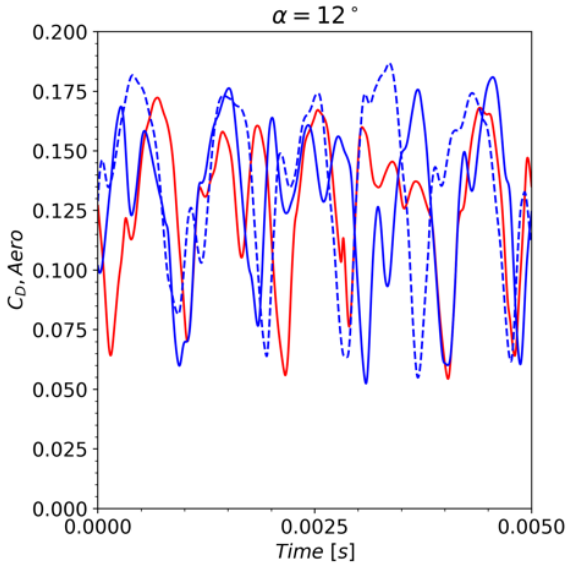

Figure 4.22: Aerodynamic drag versus time for 12° angle of attack.

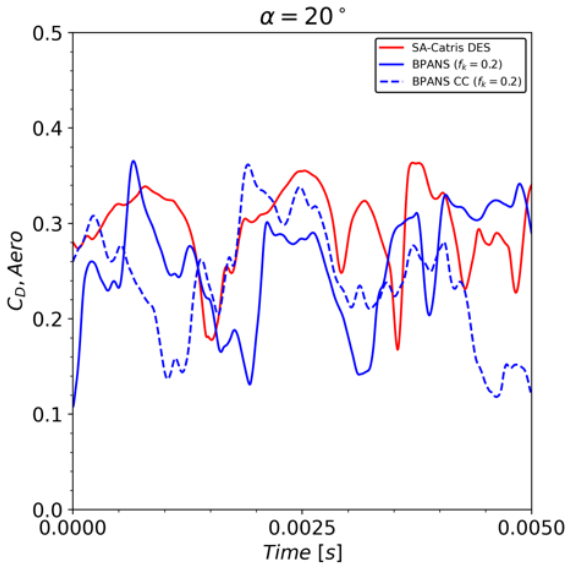

Figure 4.23: Aerodynamic drag versus time for 20° angle of attack.

SRP flow features are characterized by the experimental measurements including jet plume length (L_J), bow shock stand off distance (L_S), maximum jet plume radius (R_J), and bow shock radius (R_S). Figure 4.24 depicts these quantities visually and Table 4.1 presents current comparisons using BPANS CC against experimental results obtained from schlieren. Flow features match very well, with the simulated key quantities of interest all within 3% of experimental data. Isosurfaces of Q-criterion are presented for the three angles of attack in Figure 4.25. The increased turbulence and loss of symmetry at higher angles of attack is clearly visible in the isosurfaces and follows the vehicle drag trends plotted in Figures 4.21-4.23.

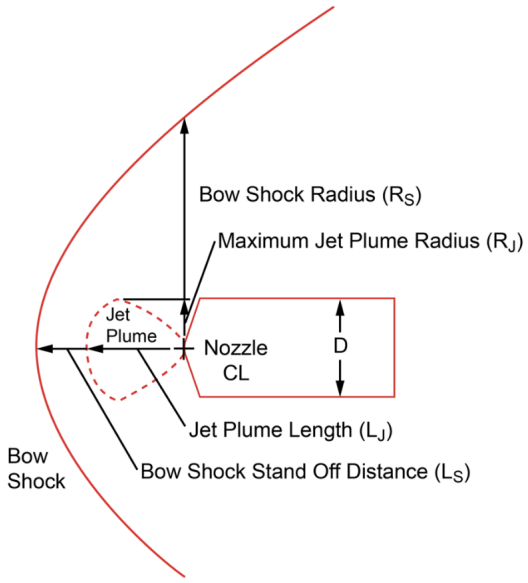

Figure 4.24: Geometrical flow feature schematic for the SRP configuration.

Table 4.1: SRP flow features compared to experimental data.

Case / Flow Feature	L_S [m]	R_S [m]	L_J [m]	R_J [m]
Experiment	0.183	0.246	0.129	0.077
BPANS	0.182	0.245	0.126	0.076

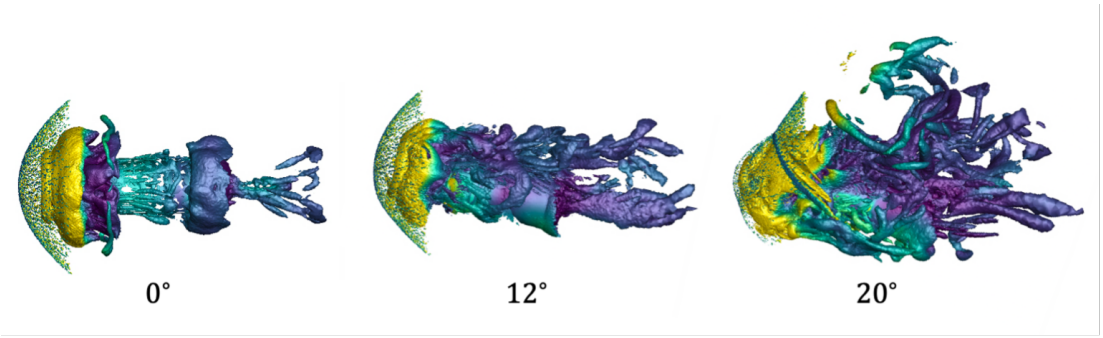

Figure 4.25: Q-criterion isosurfaces (15,000 1/s) for the three angles of attack for BPANS CC ($f_k = 0.2$) colored by pressure.

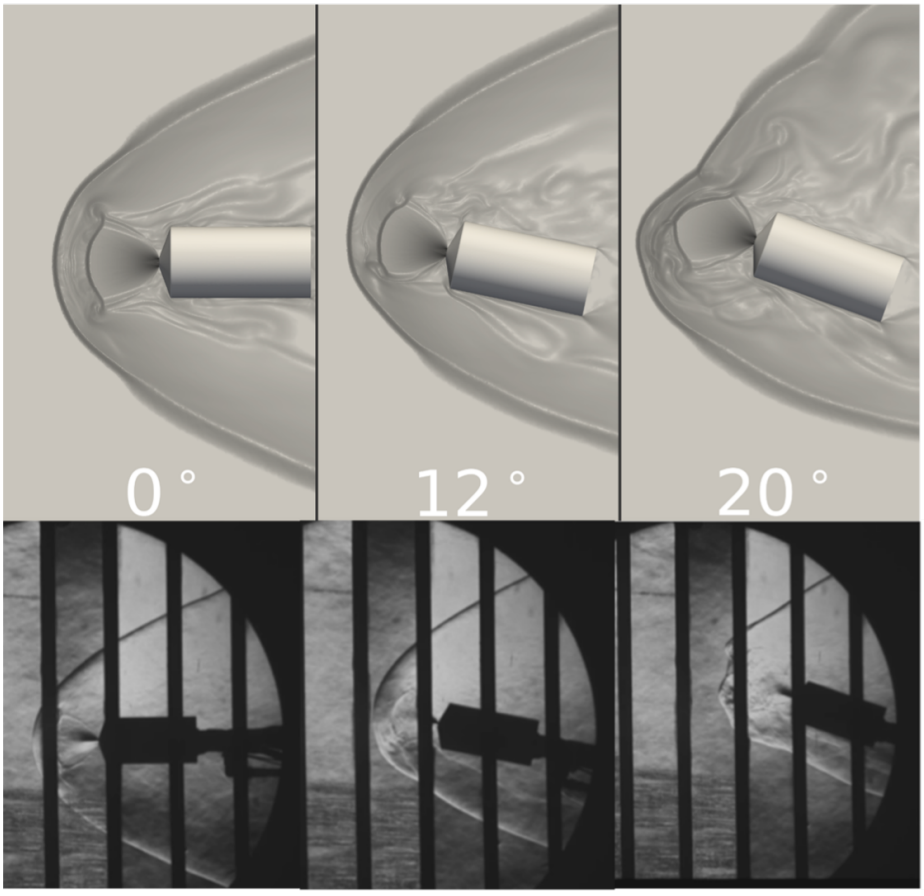

Figure 4.26: Top: Log of density gradient centerline contours for BPANS CC model. Bottom: Experimental schlieren.

Numerical schlieren are shown in Figure 4.26 with comparison to experimental schlieren [26]. As previously mentioned, the wind tunnel is not modeled and thus boundary layer turbulence and consequently density fluctuations in the farfield are not present in the simulations. In addition, the numerical schlieren generated here are centerline slices based on density gradient magnitudes and not a volume integration of the whole flowfield and schlieren direction. Nonetheless, the numerical and experimental schlieren match extremely well.

The turbulent kinetic energy spectrum at one vertical radius (near the transition lip) from the nozzle exit is plotted in Figure 4.27 using BPANS CC results for the 0° angle of attack case. An incompressible assumption is employed for the spectrum computation in which density fluctuations are neglected. The inertial subrange slope follows Kolmogorov's hypothesis for incompressible flows. Overall sound pressure level (OASPL) on the surface for the three angles of attack are plotted in Figure 4.28. The 0° angle of attack case is nearly concentric as expected and has the lowest OASPL with a mean around 140 dB on the nose. The 12° angle of attack case has larger OASPL at around 155 dB, with the highest angle of attack having the highest OASPL at around 160 dB, both maximums occurring on the windward side and the impingement point downstream. Pressure spectra are presented in Figures 4.29 and 4.30. Pressure tap data at experimental [78] probe locations are recorded every 20 time steps to match the experimental recording rate of 20 μs. Both SA-Catris and BPANS CC spectra results are computed. The models are comparable, with SA-Catris predicting slightly lower dominant frequencies than BPANS CC. Both models predict two peak frequencies.

The CFD is only run for 10 ms whereas the experiment is run for many seconds, so the vast difference in temporal scales must be considered when comparing results. In addition, CFD time-steps must be small enough to capture higher frequencies, hence the absence of the higher frequency peaks; 6.6 kHz and 8.8 kHz; shown on the experimental spectrum from the CFD results. In terms of dominant frequency prediction for the 0° angle of attack case, BPANS CC best predicts the experimental frequency of 2.2 kHz at 2.0 kHz, with SA-Catris DES predictions at 1.9 kHz. There are also still uncertainties regarding the impact of the experimental wind tunnel geometry on these frequency results (for example, impact of freestream conditions and turbulence on the shock dynamics). Overall, the results compare favorably to past simulations in literature [25, 79].

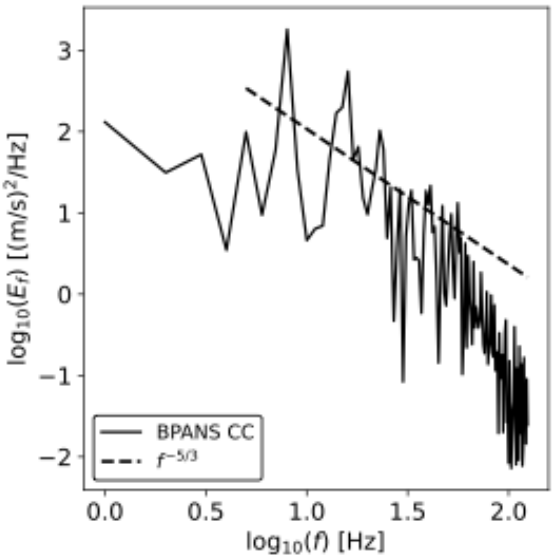

Figure 4.27: Turbulent kinetic energy spectrum at y/R = 1.

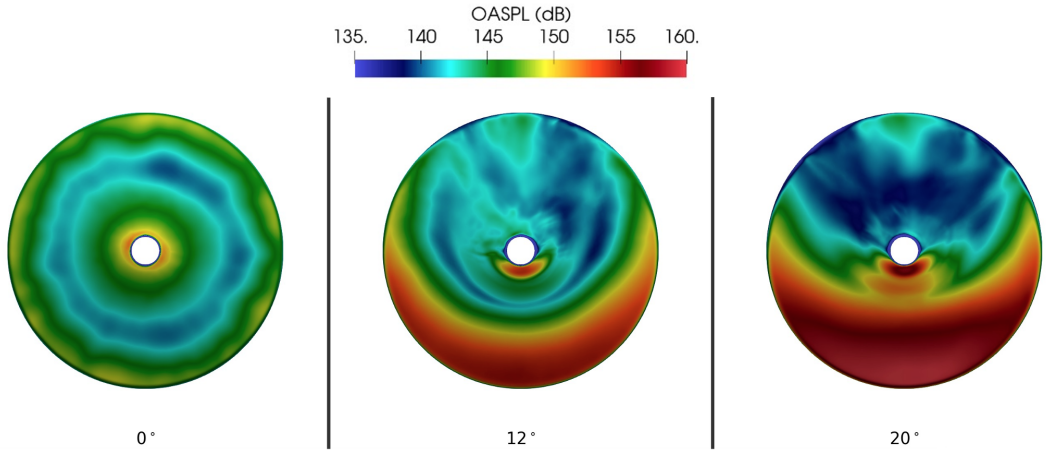

Figure 4.28: Overall Sound Pressure Level (OASPL) in decibels on the nose of the vehicle for the three angles of attack for BPANS CC ($f_k = 0.2$).

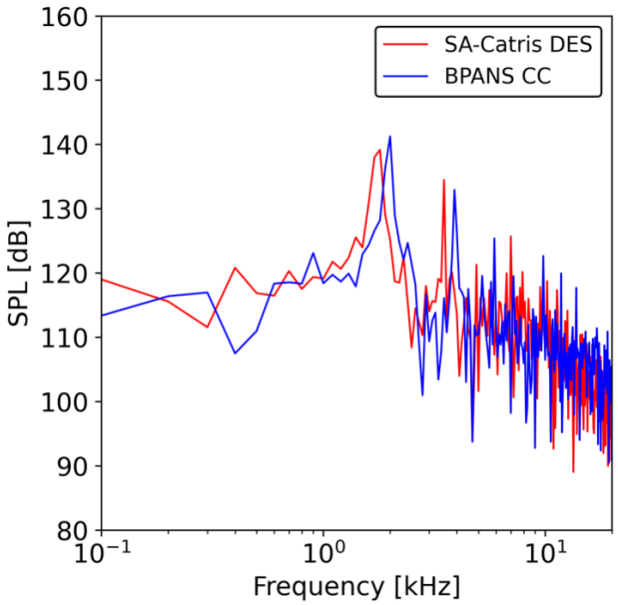

Figure 4.29: Pressure spectra plot for BPANS CC ($f_k = 0.2$) and SA-Catris DES.

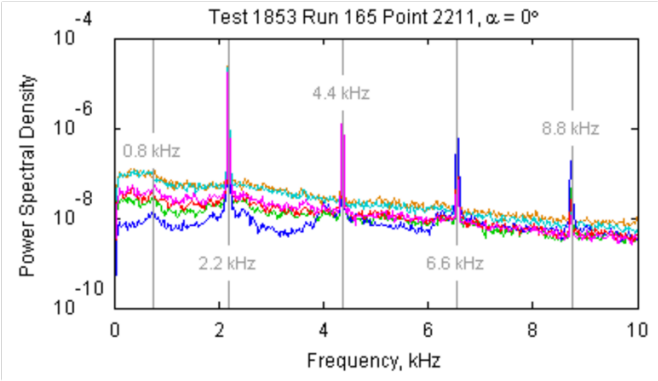

Figure 4.30: Experimental pressure spectra plot.

4.2.3 Supersonic Retropropulsion Flows with Chemistry

The following work investigates the previously described SRP configuration that has been examined experimentally for perfect gas air in the past [26]. The goal of this work is to investigate this same configuration but scaled to Martian conditions. Various gas modeling approaches are considered to determine the impacts on vehicle design. These models include perfect gas CO_2, two perfect gas pseudo species (one representing the exhaust and another for the freestream), and a 10-species chemical mechanism used in past SRP studies in literature [21, 80] to model the afterburning of the engine plumes. The Martian conditions match various similarity parameters to the air conditions including Mach number and engine pressure ratio. Temperature ratios are larger to match realistic engine temperatures; these larger ratios are not expected to significantly impact forces and moments and flow structures [23]. The supersonic retropropulsion configuration is described along with the gas models considered. Results are presented for the various gas models with key quantities of interests compared.

A perfect gas SRP experimental configuration [26] is investigated with various gas modeling approaches. The experimental conditions are as follows. The freestream Mach number is 4.6 and the freestream Reynolds number per meter is 5 million ($Re_D \approx 6 \times 10^5$). The heat shield is a 70-degree sphere cone with a diameter of 5 inches. The engine exit diameter, D_e, is 0.5 inches. The nozzle exit-to-throat area ratio is 4. The thrust coefficient is $C_T = 0.94$.

Past work investigated a family of grids with varying refinement [37]. A steady state RANS simulation refinement study demonstrated grid convergence with the family of grids. Figure 4.31 depicts the target grid consisting of 80 million cells and 15 million points. A prismatic boundary layer with target $y^+ = 1$ spacing on the vehicle heat shield is generated, with the farfield grid generated with tetrahedra. There is an engine spacing source of $\Delta/D_e = 0.04$. A spherical source outside the nozzle exit and surface has a spacing of $\Delta/D_e = 0.15$. Farfield spacing is set to $\Delta/D_e = 0.4$.

The air configuration is scaled to Martian conditions for this numerical study. The freestream Martian conditions are $\rho_\infty = 0.007$ kg/m^3, $u_\infty = 1076$ m/s, and $T_\infty = 216.53$ K. The freestream Mach number is $M_\infty = 4.6$. The atmosphere is assumed to be composed of 97% CO_2 and 3% N_2 by mass. Walls are modeled as isothermal ($T_w/T_\infty = 8$), non-catalytic, and no-slip. The engine conditions are set to $p_0 = 9.17$ bar and $T_0 = 3440$ K. These conditions lead to a thrust coefficient of approximately $C_T = 0.90$, to closely match the air experiment. The geometry is scaled up to a realistic Mars lander size; the diameter is scaled to 16.4 meters to match existing Mars lander concepts [33]. This scaling

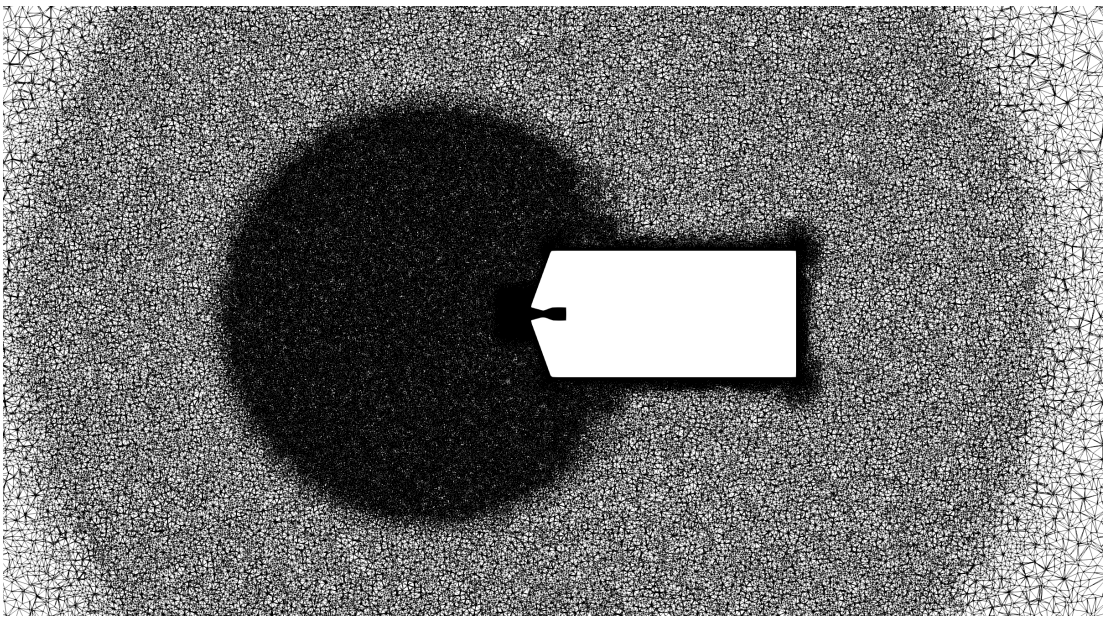

Figure 4.31: Y-plane centerline slice of 15 million point unstructured SRP grid.

increases the Reynolds number based on diameter to roughly 11 million. The same configuration geometry is utilized to enable qualitative and quantitative comparison to air data.

Various gas models are considered. First, the original air experimental configuration is simulated as a baseline and to compare directly to experimental data. Past studies investigated the $C_T = 2.0$ condition with excellent experimental agreement [21]. Gas modeling strategies used in practice typically utilize pseudo species due to the computational cost of finite-rate chemistry. A single species perfect gas CO_2 model is considered with a gas consisting of a molecular weight of 43 g/mol and a specific heat ratio of 1.33. This model is suitable for perfect gas CFD solvers which do not have the capability to model species transport. The two pseudo species approach models the freestream (denoted "Fr")

and exhaust (denoted "Ex") gases as two perfect gases, a model commonly used to reduce computational cost and stiffness. The freestream gas molecular weight and specific heat ratio are 43 g/mol and 1.33, respectively. The exhaust molecular weight and specific heat ratio are 20 g/mol and 1.25, respectively. Lastly, a 10 species mechanism containing reactions to model afterburning of the exhaust post-plenum is considered. NASA CEA [81] is used to compute plenum equilibrium conditions. An oxidizer to fuel ratio of oxygen and methane of 3.5 is used along with the pressure to compute the engine chamber temperature noted previously. The equilibrium plenum mass fractions are shown in Table 4.2. The reactions considered are tabulated in Table 4.3. This model is run without reactions as well to examine differences to the two pseudo species approach which is also inert.

The time step, Δt, is set to $\tau/\Delta t = 171.0$, where $\tau = D/u_\infty$ is the reference time scale. This time step ratio is similar to past studies [25, 21] and corresponds to a CFL of O(1-5) upstream of the vehicle. In total, 15,000 time steps (five subiterations per time step) are run per case. Statistics are saved for the last 10,000 time steps. Simulations are carried out on one 8 $\times$ NVIDIA A100 GPU node. A perfect gas CO_2 model simulation takes approximately 4 hours and a 10 species model simulation takes approximately 13 hours. The reacting gas simulation is slightly faster than the expected speed which should scale with the number of equations squared (7 for the perfect gas simulation, 16 for the reacting gas simulation). The difference is attributed primarily to stronger scaling for the perfect gas simulation.

Table 4.2: Engine plenum species mass fractions.

Species	Mass Fraction
H_2O	0.34507
CO_2	0.20085
H_2	0.00960
CO	0.26016
OH	0.08473
O_2	0.07334
O	0.02363
H	0.00262

Table 4.3: Chemical mechanism used for this study. Units are in seconds, moles, cubic centimeters, calories, and Kelvin. [a]Rate coefficients are given in the form $k = AT^n e^{-T_a/T}$.

#	Reaction[a]	A	n	T_a	Factors and Reference
1	$CO + M \longleftrightarrow C + O + M$	1.2×10^{21}	-1.0	1.29×10^5	$H, C, O = 1.5$, [82]
2	$CO + O \longleftrightarrow O_2 + C$	3.9×10^{13}	-0.18	6.92×10^4	[83]
3	$CO_2 + M \longleftrightarrow CO + O + M$	6.9×10^{21}	-1.5	6.3275×10^4	$H, C, O = 2.0$, [83]
4	$CO_2 + O \longleftrightarrow O_2 + CO$	2.7×10^{14}	0.0	3.3797×10^4	[82]
5	$H + CO_2 \longleftrightarrow CO + OH$	1.6×10^{14}	0.0	1.32×10^4	[84]
6	$H + H_2O \longleftrightarrow H_2 + OH$	1.0×10^{10}	1.2	9.62×10^3	[84]
7	$H_2 + H \longleftrightarrow 2H + H$	8.5×10^{19}	-1.1	5.2335×10^4	[84]
8	$H_2 + H_2O \longleftrightarrow 2H + H_2O$	8.5×10^{19}	-1.1	5.2335×10^4	[84]
9	$H_2 + M \longleftrightarrow 2H + M$	9.0×10^{14}	0.0	4.840×10^4	$H, H_2O = 0.0$, [84]
10	$H_2 + O_2 \longleftrightarrow 2OH$	2.5×10^{12}	0.0	1.96×10^4	[84]
11	$H_2O + C \longleftrightarrow OH + H + C$	1.3×10^{21}	-1.0	6.0×10^4	[84]
12	$H_2O + H \longleftrightarrow OH + 2H$	1.3×10^{21}	-1.0	6.0×10^4	[84]
13	$H_2O + H_2O \longleftrightarrow OH + H + H_2O$	1.3×10^{21}	-1.0	6.0×10^4	[84]
14	$H_2O + M \longleftrightarrow OH + H + M$	1.3×10^{22}	-1.6	6.0×10^4	$H, C, O, H_2O = 0.0$, [84]

15	$H_2O + O \longleftrightarrow OH + H + O$	1.3×10^{21}	-1.0	6.0×10^4	[84]
16	$O + H_2 \longleftrightarrow OH + H$	3.9×10^4	2.7	3.15×10^3	[84]
17	$O + H_2O \longleftrightarrow 2\,OH$	3.4×10^{10}	1.0	8.6×10^3	[84]
18	$O_2 + M \longleftrightarrow 2\,O + M$	2.0×10^{21}	-1.5	5.936×10^4	$H, C, O = 5.0$, [85]
19	$OH + M \longleftrightarrow O + H + M$	2.4×10^{15}	0.0	5.0×10^4	[84]

Figure 4.32 plots aerodynamic drag over time for the cases investigated. All the gas models exhibited unsteady aerodynamic drag. The Martian condition simulations predict aerodynamic drag approximately double that of the experimental air simulation. The fluctuations are comparable between all the simulations. The dominant frequencies of the unsteady drag are listed in Table 4.4. The Martian simulations have larger dominant frequencies over the air experiment simulation. The dominant frequency increases as fidelity is increased, with the reacting gas model being almost two times larger than the air gas model. The impact of the specific gas model on the aerodynamic drag is minor. The aerodynamic drag is approximately 11-19% of the total drag of the vehicle which incorporates the engine thrust which is similar to past studies. Figure 4.33 plots average pressure coefficient on the heat shield and across the body length for all the models as well as experimental data. The air simulation agrees well with the experimental air data on the heat shield and slightly under predicts pres-

sure along the body. The Martian condition simulations, noted to be at roughly 20 times the Reynolds number of the air setup, predict slightly larger pressure coefficients along the heat shield and body. Peak pressures near the shoulder are slightly larger for the multi-species cases than the pure CO_2 model. The 10 species mechanism cases predict larger pressures near the radial mid point on the heat shield than the inert and pseudo species models. Along the body, all the Martian condition results lie in between the experimental data.

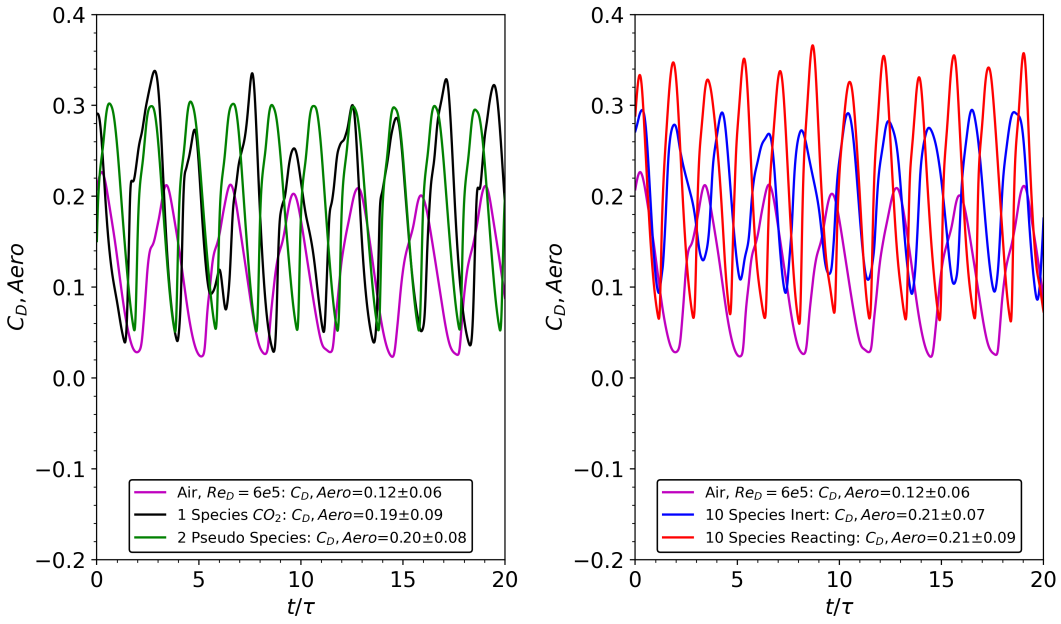

Figure 4.32: Aerodynamic drag coefficient versus non-dimensional time for the various gas models. Left: Air versus 1 and 2 species models. Right: Air versus 10 species models.

Table 4.4: SRP dominant force frequencies for the various gas models.

Case	f $[1/s^*]$
Air	0.32
1 Species CO_2	0.42
2 Species	0.50
10 Species Inert	0.49
10 Species Reacting	0.58

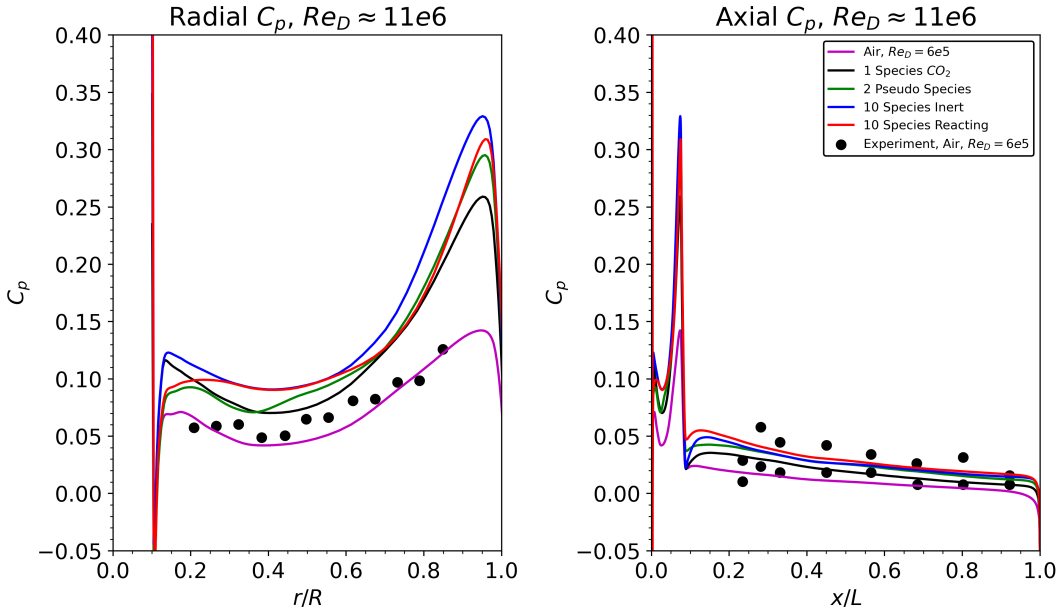

Figure 4.33: Mean axial and radial pressure coefficient for the various gas models. Air experiment data are shown for reference.

The plume characteristics shown in Figure 4.24 are measured from mean pressure contours computed on a Y-plane centerline slice of the domain. Specifically, jet plume length (L_J), bow shock stand-off distance (L_S), maximum jet plume radius (R_J), and bow shock radius (R_S) are measured for each model and compared against experimental data [26] in Table 4.5. The air simulation compares very well to the experimental results. Errors in experimental values range from 2-6%. The Martian condition simulations generally predict slightly smaller plumes. Plume structures are a stronger function of the specific heat ratio for inert flows. Specific heat ratio differs significantly versus air experiments as seen visually in Figure 4.36 which plots specific heat ratio contours. The reacting gas model predicted the smallest plumes, predicting length ratios about 70-80% of the experimental ratio besides the maximum jet plume ratio which is consistent across all the gas models. Figure 4.34 plots schlieren for the experiment and pseudo schlieren (slice of log of density gradient magnitude) for the air simulation. The geometric agreement presented in Table 4.5 between the experiment and simulation are clearly visible.

Table 4.5: SRP flow features compared to experimental air data.

Case / Flow Feature	L_S/R	R_S/R	L_J/R	R_J/R
Experiment (Air)	2.14	2.79	1.48	0.78
Air	2.09	2.85	1.39	0.75
1 Species CO_2	1.94	2.41	1.26	0.71
2 Species	1.80	2.48	1.22	0.75
10 Species Inert	1.80	2.41	1.22	0.74
10 Species Reacting	1.60	2.32	1.06	0.78

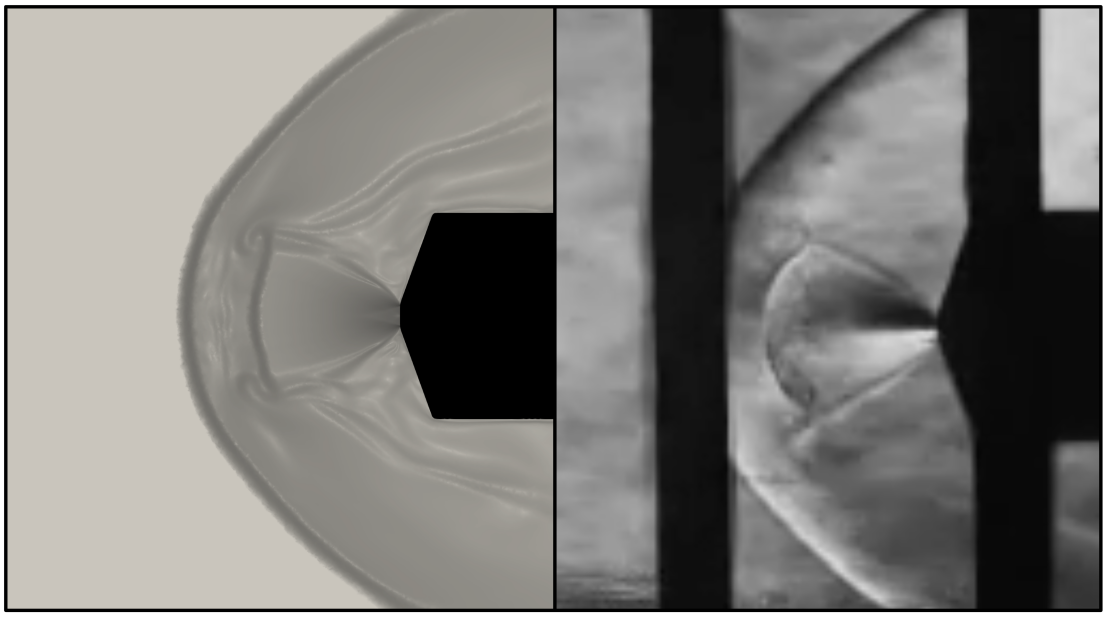

Figure 4.34: Left: Air simulation pseudo schlieren (log of density gradient magnitude). Right: Experimental schlieren.

Contours for the Martian conditions are plotted in Figures 4.35-4.36. Instantaneous Mach number shown in Figure 4.35 is similar across most gas models, but is slightly lower in the plumes for the reacting gas model due to larger plume temperatures due to the chemistry. Instantaneous species mass fractions are plotted in Figure 4.35. In the multi-species models, the vehicle body is completely surrounded by the engine exhaust for this configuration. The differences between inert and reacting chemistry is also apparent in the H_2O mass fraction; more H_2O is present for the reacting gas model, notably in the core plume. Instantaneous specific heat ratio contours are plotted in Figure 4.36. The specific heat ratios for the 10 species models vary substantially in the flow fields. The specific heat ratios are smaller in the reacting gas model due to larger predicted plume temper-

atures over the inert gas model. Pseudo species models should likely incorporate temperature dependence to better predict flow properties in the plumes. Average temperature in Kelvin is plotted in Figure 4.36. Qualitatively, the inert gas models predict similar temperature profiles. The temperature upstream of the Mach disk reaches stagnation temperatures comparable to the plenum temperature. These regions of high temperature are larger for the inert models. The reacting model predicts significantly larger internal plume temperatures and has a smaller high temperature region at the stagnation point due to the chemical reactions.

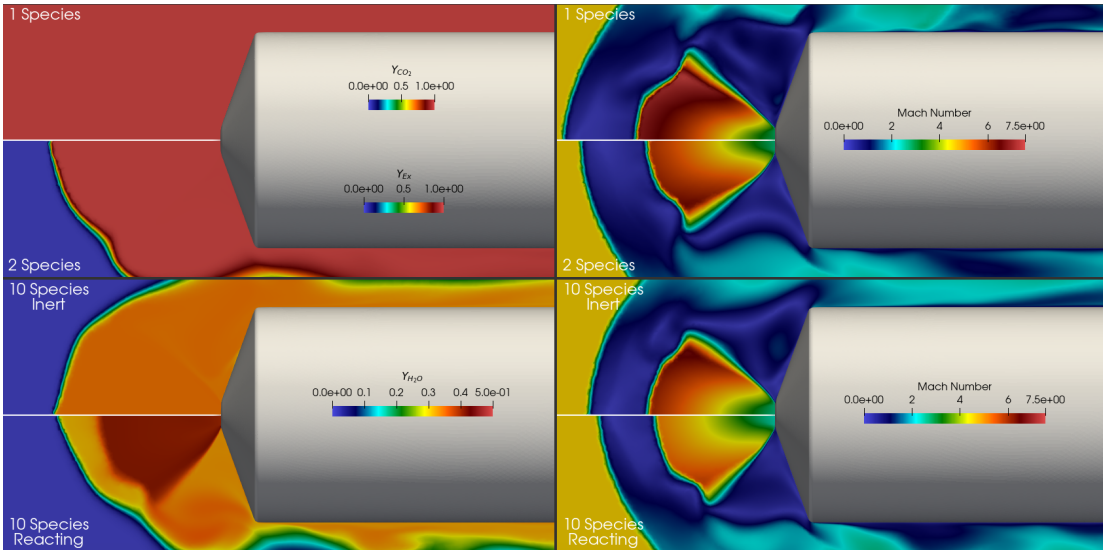

Figure 4.35: Contours on a Y-plane centerline slice for the various gas models. Left: Instantaneous species. Right: Instantaneous Mach number.

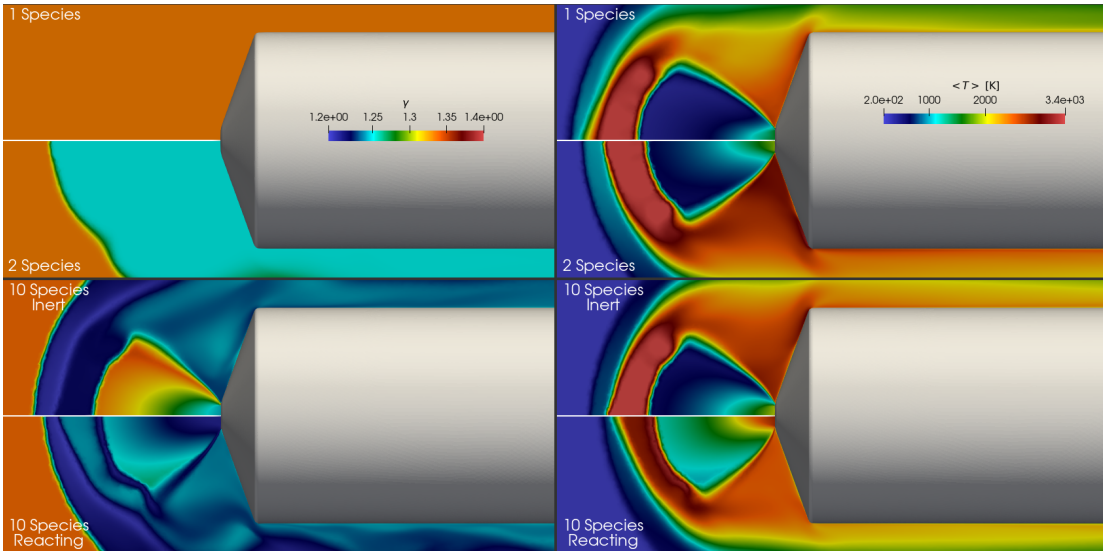

Figure 4.36: Contours on a Y-plane centerline slice for the various gas models. Left: Instantaneous specific heat ratio. Right: Mean temperature in Kelvin.

Various turbulent quantities are plotted on the centerline slice in Figure 4.37 for the reacting gas model. The quantities are split between resolved and modeled quantities. The resolved turbulent Mach number, computed using the resolved turbulent kinetic energy, $\frac{1}{2}\widetilde{u_i'' u_i''}$, peaks around one at the plume triple point, and is of order half in the shear layer and recirculation regions. The modeled turbulent Mach number peaks around half in the recirculation region. The resolved turbulent kinetic energy is largest at the plume triple point and the heat shield shoulder which is also qualitatively observed in the experimental schlierens for the air setup [26]. The mean turbulent viscosity ratio peaks around 350 in the recirculation region. Taking the total turbulent kinetic energy as the sum of the resolved and modeled components, the underresolved ratio is primarily in the recirculation region and peaks around 50%, with most of the region around

25%. At the triple point, where resolved turbulent kinetic energy is largest, this ratio is below 5%.

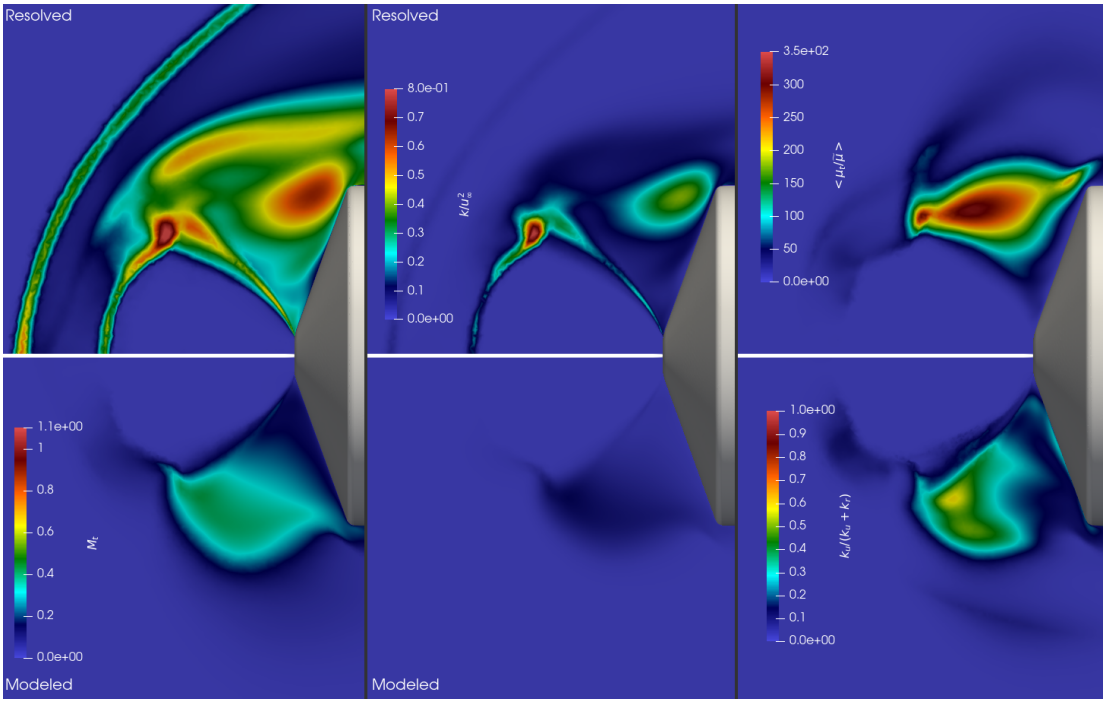

Figure 4.37: Various turbulent related contours on a Y-plane centerline slice for the reacting gas model. Left: Turbulent Mach number. Middle: Non-dimensional turbulent kinetic energy. Right: Average turbulent viscosity ratio and underresolved (or modeled) turbulent kinetic energy ratio. Resolved and modeled quantities are denoted on the first two columns.

Overall sound pressure level (OASPL), using a reference sound pressure of 20 μPa, on the surface for the four gas models are plotted in Figure 4.38. All the models predict nearly concentric contours as expected. The inert and pseudo species gas models predict the lowest OASPL on the surface at around 135 dB at $r/R \approx 0.3$. The single species CO_2 gas model predicts the largest OASPL at this same radial location with an OASPL of 140 dB. The peaks occur at the

shoulder for all models similarly to the air experiments. The reacting gas model predicts the smallest OASPL near the nozzle compared to all other models, but predicts the largest OASPL near the shoulder. The normalized radial pressure fluctuations are plotted in Figure 4.39. The fluctuations near the engine exit are one to two times the mean pressure for all gas models. Near the shoulder, the fluctuations are roughly half the magnitude of the overall pressure. These fluctuations ultimately drive the overall force profile and would not be possible to predict with RANS models, emphasizing the need for scale-resolving simulations.

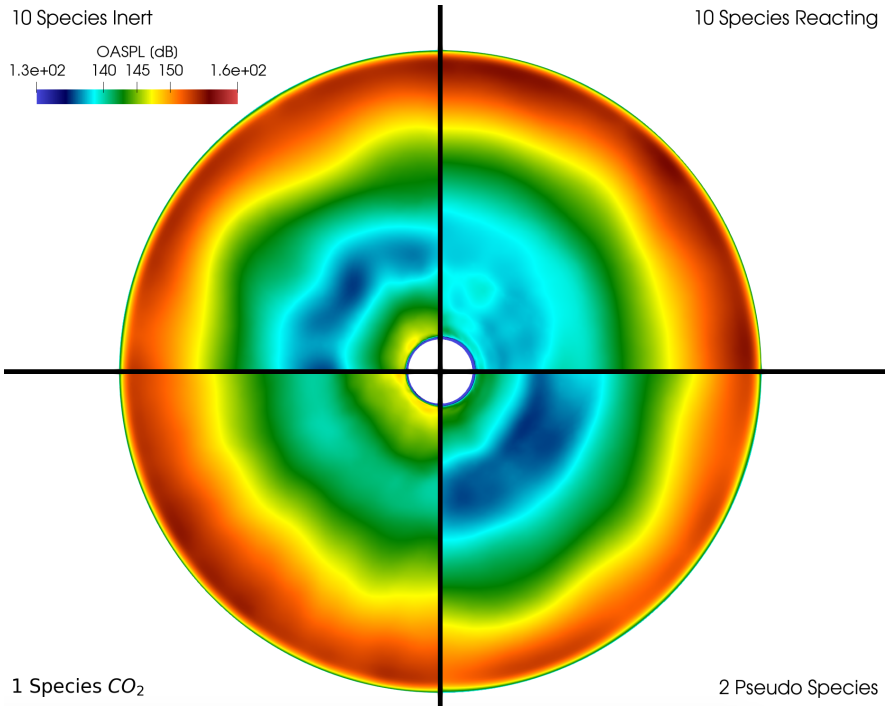

Figure 4.38: Overall Sound Pressure Level (OASPL) in decibels on the nose of the vehicle for the four gas models. Each 90° pane plots a different gas model.

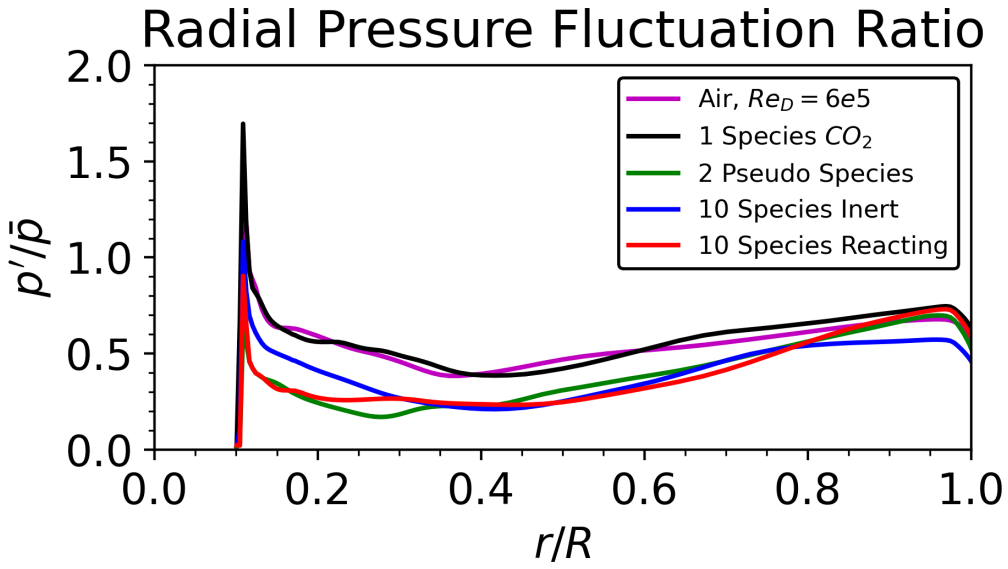

Figure 4.39: Normalized pressure fluctuations (by the average pressure) on the nose of the vehicle.

Axial line plots of the mean temperature for the various gas models are plotted in Figure 4.40. The smaller plume length is visible for the reacting gas model. The reaction zone upstream of the Mach disk is also clearly pronounced. All the inert models predict similar temperature profiles. Axial line plots of various mean mass fractions are plotted in Figure 4.41 for the reacting and inert gas models. The reaction zone begins with the production of CO and OH ahead of the Mach disk due to the temperature rising. The reduction of CO_2 and H_2O is also present in the reaction zone.

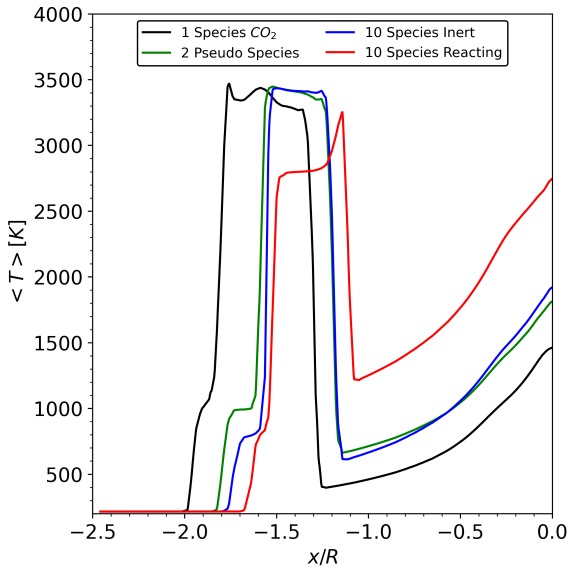

Figure 4.40: Mean temperature versus axial distance for the various gas models. The engine exit is zero.

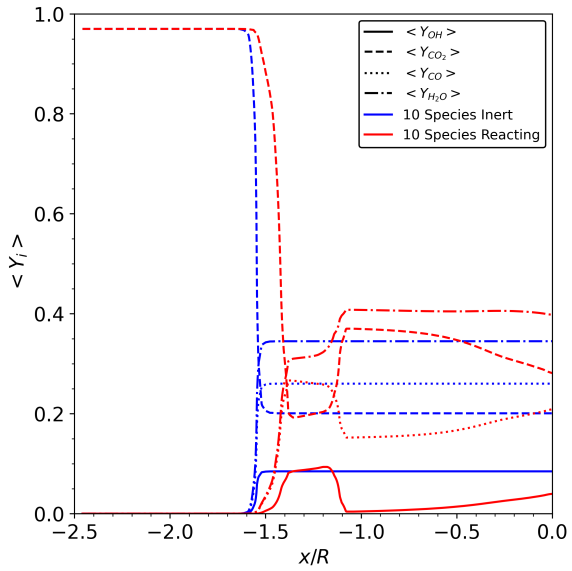

Figure 4.41: Various mean mass fractions versus axial distance for inert and reacting models. The engine exit is zero.

Chapter 5. Conclusions and Future Work

5.1 Conclusions

The scale resolving BPANS turbulence model has been extended to high-speed compressible flows leading to a new model called BPANS CC (compressibility corrected). The new model has been demonstrated on both a canonical high-speed compressible mixing layer flow and a canonical SRP configuration with successful comparisons to experimental data. The model also compares favorably to other unsteady modeling approaches such as DES. The model is capable of matching supersonic mixing layer mixing curves and growth rates. For the complex SRP configuration, BPANS CC adequately predicts experimental surface data and geometrical flow features. It is found that compressibility corrections improved predictions over the non-corrected cases. The corrections led to improved surface pressure predictions on the heat shield of the vehicle at higher angles of attack.

A numerical investigation of varying gas models has also been carried out on the SRP configuration. Five gas modeling approaches were investigated: air, pure CO_2, 2 pseudo species, and inert and reacting 10 species models. The air gas model is used to simulate the experimental air configuration and compares favorably to experimental pressure and schlieren data. The other gas models

are used to simulate a Martian condition. In terms of aerodynamic drag, all the Martian gas models predict similar average drag coefficients as well as fluctuations, although approximately double that of the air configuration. Plume structure length ratios vary up to 30% versus the experimental air configuration, attributed primarily to significant specific heat ratio and composition changes in the plumes. These simulations have been carried out on a single GPU node and are individually capable of being run overnight. As the computational cost of the reacting gas simulation is only three times as expensive than that of the single species simulation, the reacting gas model seems to be the best modeling approach due to reduced approximations. The pseudo species approach predicts nearly identical drag and similar plume length ratios versus the reacting gas model and is useful if quicker turn around is needed.

As unsteady compressible flow simulations continue to play a larger role in design of aerospace systems, BPANS shows promise as a turbulence model to accurately predict unsteady flow features and loads. BPANS has also been demonstrated using unstructured grids and implicit time stepping on next-generation GPU hardware which is important as HPC moves toward GPUs in the near future. The combination of BPANS and BPANS CC provides an opportunity to simulate unsteady turbulent flows from low subsonic to hypersonic speeds at low computational cost and a reasonable accuracy versus higher fidelity methods such as LES and DNS.

5.2 Future Work

There are various avenues for future work which are inherent to unsteady simulation in general. One key area moving forward is adaption in both the PANS parameters and the grid. One primary issue with the current approach is ensuring that the spatial and temporal resolutions are adequate for the specified underresolved-to-total ratios. Using constant parameters enables distinction between numerical and modeling errors. In the limit of fine grid, results will, in theory, grid converge. Adaptive grids can reduce numerical error. Adaptive mesh refinement is becoming more common place for steady state simulations, but still is a challenge for unsteady problems with respect to computational cost. Time-dependent AMR is ultimately desired. High order spatial and temporal methods are also desirable for unsteady turbulent flow simulations. Efficient implicit time integration for high order methods is still an open research problem. Curved mesh boundaries and curved mesh adaptation are also problems that must be eventually solved. Extension of PANS to utilize wall-models can alleviate some of the issues noted above for flows with minimal separation, but most flows where unsteady flow simulations are required involve large separation where wall-model validity is questionable.

In terms of SRP, retropropulsion experiments involving chemistry and more similar environments to Mars are desired for additional data and validation of such modeling approaches used for Mars lander retropropulsion concepts. Relaxation of the plenum equilibrium assumption is also an avenue of future

physics extensions. Engines with injectors enable higher fidelity simulations and the capability to predict thermoacoustic instabilities that can occur as well as throttling in a more physics-based manner.

References

[1] Parviz Moin and John Kim. Tackling turbulence with supercomputers. *Scientific American*, 276(1):62–68, 1997.

[2] W Peter Jones and Brian Edward Launder. The prediction of laminarization with a two-equation model of turbulence. *International Journal of Heat and Mass Transfer*, 15(2):301–314, 1972.

[3] David C Wilcox. Reassessment of the scale-determining equation for advanced turbulence models. *AIAA Journal*, 26(11):1299–1310, 1988.

[4] Florian R Menter. Two-equation eddy-viscosity turbulence models for engineering applications. *AIAA Journal*, 32(8):1598–1605, 1994.

[5] Philippe Spalart and Steven Allmaras. A one-equation turbulence model for aerodynamic flows. In *30th Aerospace Sciences Meeting and Exhibit 1992-439*, 1992.

[6] Stéphane Catris and Bertrand Aupoix. Density corrections for turbulence models. *Aerospace Science and Technology*, 4(1):1–11, 2000.

[7] Joseph Smagorinsky. General circulation experiments with the primitive equations: I. the basic experiment. *Monthly Weather Review*, 91(3):99–164, 1963.

[8] TS Lund. The use of explicit filters in large eddy simulation. *Computers & Mathematics with Applications*, 46(4):603–616, 2003.

[9] Stephen B Pope. Turbulent flows. *Measurement Science and Technology*, 12(11):2020–2021, 2001.

[10] Stephen B Pope. Ten questions concerning the large-eddy simulation of turbulent flows. *New Journal of Physics*, 6(1):35, 2004.

[11] Gabriel Nastac, Jeffrey W Labahn, Luca Magri, and Matthias Ihme. Lyapunov exponent as a metric for assessing the dynamic content and predictability of large-eddy simulations. *Physical Review Fluids*, 2(9):094606, 2017.

[12] Haecheon Choi and Parviz Moin. Grid-point requirements for large eddy simulation: Chapman's estimates revisited. *Physics of Fluids*, 24(1), 2012.

[13] Philippe R Spalart. Comments on the feasibility of LES for wings, and on a hybrid RANS/LES approach. In *Proceedings of First AFOSR International Conference on DNS/LES*, pages 137–147. Greyden Press, 1997.

[14] Sanjeeb T Bose and George Ilhwan Park. Wall-modeled large-eddy simulation for complex turbulent flows. *Annual Review of Fluid Mechanics*, 50:535–561, 2018.

[15] Sharath S Girimaji, Ravi Srinivasan, and Euhwan Jeong. PANS turbulence model for seamless transition between RANS and LES: fixed-point analysis and preliminary results. In *Fluids Engineering Division Summer Meeting*, volume 36975, pages 1901–1909, 2003.

[16] Sharath S Girimaji. Partially-Averaged Navier-Stokes model for turbulence: A Reynolds-Averaged Navier-Stokes to Direct Numerical Simulation bridging method. *Journal of Applied Mechanics*, 2006.

[17] Philippe R Spalart. Detached-eddy simulation. *Annual Review of Fluid Mechanics*, 41:181–202, 2009.

[18] Charles G Speziale. Turbulence modeling for time-dependent rans and vles: a review. *AIAA Journal*, 36(2):173–184, 1998.

[19] Hosein Foroutan and Savas Yavuzkurt. A partially-averaged Navier-Stokes model for the simulation of turbulent swirling flow with vortex breakdown. *International Journal of Heat and Fluid Flow*, 50:402–416, 2014.

[20] Abdelkader Frendi and Christopher Harrison. Partially Averaged Navier-Stokes: A (k-ω)/(k-ε) bridging model. *Fluids*, 5(3):129, 2020.

[21] Gabriel Nastac and Abdelkader Frendi. An investigation of scale-resolving turbulence models for supersonic retropropulsion flows. *Fluids*, 7(12):362, 2022.

[22] Alicia M. Dwyer-Cianciolo, Tara Polsgrove, Ronald R. Sostaric, Karl T. Edquist, Ashley M. Korzun, and Joseph A. Garcia. Human Mars entry,

descent, and landing architecture study: Phase 3 summary. In *AIAA Paper 2021-1509*, 2021.

[23] Ashley M Korzun, Juan R Cruz, and Robert D Braun. A survey of supersonic retropropulsion technology for Mars entry, descent, and landing. *Journal of Spacecraft and Rockets*, 46(5):929–937, 2009.

[24] Kerry Trumble. An initial assessment of Navier-Stokes codes applied to supersonic retro-propulsion. In *AIAA Paper 2010-5047*, 2010.

[25] Daniel Schauerhamer, Kerry Trumble, William Kleb, Jan-Reneé Carlson, and Karl Edquist. Continuing validation of computational fluid dynamics for supersonic retropropulsion. In *AIAA Paper 2012-864*, 2012.

[26] Scott A Berry and Matthew N Rhode. Supersonic retropropulsion test 1853 in NASA LaRC Unitary Plan wind tunnel test section 2. *NASA/TP-2014-218256*, 2014.

[27] Hicham Alkandry. *Aerodynamic Interactions of Propulsive Deceleration and Reaction Control System Jets on Mars-Entry Aeroshells.* PhD thesis, University of Michigan, 2012.

[28] Pratibha Raghunandan, Jeffrey Hill, Stephen M Ruffin, and Suman Muppidi. Aerothermal and aerodynamic characterization of reacting jets for supersonic retropropulsive missions to Mars. In *AIAA Paper 2018-3766*, 2018.

[29] Karl T Edquist, Ashley M Korzun, Karen Bibb, Daniel G Schauerhamer, Edward C Ma, Peter L McCloud, Grant E Palmer, and Joshua D Monk. Comparison of Navier-Stokes flow solvers to Falcon 9 supersonic retropropulsion flight data. In *AIAA Paper 2017-5296*, 2017.

[30] Tobias Ecker, Franziska Zilker, Etienne Dumont, Sebastian Karl, and Klaus Hannemann. Aerothermal analysis of reusable launcher systems during retropropulsion reentry and landing. In *Space Propulsion Conference Paper 2018-40*, 2018.

[31] Tobias Ecker, Sebastian Karl, Etienne Dumont, Sven Stappert, and Daniel Krause. Numerical study on the thermal loads during a supersonic rocket retropropulsion maneuver. *Journal of Spacecraft and Rockets*, 57(1):131–146, 2020.

[32] Ashley M. Korzun, Eric Nielsen, Aaron Walden, William Jones, Jan-Renee Carlson, Patrick Moran, Christopher Henze, and Timothy Sandstrom. Computational investigation of retropropulsion operating environments with a massively parallel detached eddy simulation approach. In *AIAA Paper 2020-4228*, 2020.

[33] Karl T Edquist, Ashley M Korzun, William L Kleb, Veronica Hawke, Yehia M Rizk, Michael E Olsen, and Francisco Canabal. Model design and pre-test CFD analysis for a supersonic retropropulsion wind tunnel test. In *AIAA Paper 2020-2230*, 2020.

[34] ORNL. Summit. `https://www.olcf.ornl.gov/olcf-resources/compute-systems/summit`, 2020.

[35] Karl T Edquist, Stephen J Alter, Christopher E Glass, William L Kleb, Ashley M Korzun, William A Wood, Francisco Canabal, Robert Childs, Logan D Halstrom, and Kristen V Matsuno. Computational modeling of Mars retropropulsion concepts in the Langley Unitary Plan wind tunnel. In *AIAA Paper 2022-0912*, 2022.

[36] Justin Shafner and Ashley M. Korzun. Computational analysis of a multiple-nozzle supersonic retropropulsion configuration. In *AIAA Paper 2021-2556*, 2021.

[37] Gabriel Nastac, Ashley M Korzun, Aaron Walden, Eric J Nielsen, William T Jones, and Patrick Moran. Computational investigation of the effect of chemistry on Mars supersonic retropropulsion environments. In *AIAA Paper 2022-2299*, 2022.

[38] Gabriel Nastac, Aaron Walden, Eric J Nielsen, and Abdelkader Frendi. Implicit thermochemical nonequilibrium flow simulations on unstructured grids using GPUs. In *AIAA Paper 2021-0159*, 2021.

[39] Gabriel Nastac, Aaron Walden, Li Wang, Eric J Nielsen, Yi Liu, Matthew Opgenorth, Jason Orender, and Mohammad Zubair. A multi-architecture approach for implicit computational fluid dynamics on unstructured grids. In *AIAA Paper 2023-1226*, 2023.

[40] Gabriel Nastac and Abdelkader Frendi. Numerical investigation of gas models for retropropulsion flows for future Mars missions. *Under Review*, 2024.

[41] David C Wilcox et al. *Turbulence modeling for CFD*, volume 2. DCW Industries, 1998.

[42] Bonnie J McBride, Sanford Gordon, and Martin A Reno. Coefficients for calculating thermodynamic and transport properties of individual species. *NASA TM 4513*, 1993.

[43] Joseph Boussinesq. *Essai sur la théorie des eaux courantes*. Impr. nationale, 1877.

[44] Peter A Gnoffo, Roop N Gupta, and Judy L Shinn. *Conservation Equations and Physical Models for Hypersonic Air Flows in Thermal and Chemical Nonequilibrium*. NASA TP 2867, 1989.

[45] Christopher L Rumsey. Compressibility considerations for $k-\omega$ turbulence models in hypersonic boundary-layer applications. *Journal of Spacecraft and Rockets*, 47(1):11–20, 2010.

[46] Yildirim Suzen and Klaus Hoffmann. Investigation of supersonic jet exhaust flow by one-and two-equation turbulence models. In *36th AIAA Aerospace Sciences Meeting and Exhibit*, page 322, 1998.

[47] William K Anderson, Robert T Biedron, Jan-Reneé Carlson, Joseph M Derlaga, Cameron T Druyor Jr, Peter A Gnoffo, Dana P Hammond, Kevin E Jacobson, William T Jones, Bil Kleb, Elizabeth M Lee-Rausch, Yi Liu, Gabriel C. Nastac, Christopher L. Rumsey, James L. Thomas, Kyle B. Thompson, Aaron C. Walden, Li Wang, Stephen L. Wood, William A. Wood, and Xinyu Zhang. *FUN3D Manual: 14.0.2*. NASA TM 20230004211, 2023.

[48] Thomas Gerhold, M Galle, O Friedrich, J Evans, T Gerhold, M Galle, O Friedrich, and J Evans. Calculation of complex three-dimensional configurations employing the DLR-TAU-code. In *35th Aerospace Sciences Meeting and Exhibit*, page 167, 1997.

[49] Thomas D Economon, Francisco Palacios, Sean R Copeland, Trent W Lukaczyk, and Juan J Alonso. SU2: An open-source suite for multiphysics simulation and design. *AIAA Journal*, 54(3):828–846, 2016.

[50] Philip L Roe. Approximate Riemann solvers, parameter vectors, and difference schemes. *Journal of Computational Physics*, 43(2):357–372, 1981.

[51] Gabriel Nastac, Robert Tramel, and Eric J Nielsen. Improved heat transfer prediction for high-speed flows over blunt bodies using adaptive mixed-element unstructured grids. In *AIAA Paper 2022-0111*, 2022.

[52] C.O.E. Burg. Higher order variable extrapolation for unstructured finite volume RANS flow solvers. In *AIAA Paper 2005-4999*, 2005.

[53] Bram Van Leer. Towards the ultimate conservative difference scheme. v. a second-order sequel to Godunov's method. *Journal of Computational Physics*, 32(1):101–136, 1979.

[54] Sigal Gottlieb, Chi-Wang Shu, and Eitan Tadmor. Strong stability-preserving high-order time discretization methods. *SIAM review*, 43(1):89–112, 2001.

[55] Mohammad Zubair, Eric Nielsen, Justin Luitjens, and Dana Hammond. An optimized multicolor point-implicit solver for unstructured grid applications on graphics processing units. In *2016 6th Workshop on Irregular Applications: Architecture and Algorithms (IA3)*, pages 18–25. IEEE, 2016.

[56] Aaron Walden, Eric Nielsen, Boris Diskin, and Mohammad Zubair. A mixed precision multicolor point-implicit solver for unstructured grids on GPUs. In *2019 IEEE/ACM 9th Workshop on Irregular Applications: Architectures and Algorithms (IA3)*, pages 23–30. IEEE, 2019.

[57] Kincade, Kathy. Berkeley Lab, Oak Ridge, NVIDIA Team Breaks Exaop Barrier With Deep Learning Application. `https://www.nersc.gov/news-publications/nersc-news/science-news/2018/berkeley-lab-oak-ridge-nvidia-team-breaks-exaop-barrier-with-deep-learning-application/`, 2018. Last Accessed January 1, 2024.

[58] E. Strohmaier, J. Dongarra, H. Simon, M. Meuer, and H. Meuer. The Top 500 List. `http://www.top500.org`, 2020. Last Accessed January 1, 2024.

[59] Rick Stevens, Jini Ramprakash, Paul Messina, Michael Papka, and Katherine Riley. Aurora: Argonne's next-generation exascale supercomputer. Technical report, Argonne National Laboratory, 2019.

[60] ORNL. Frontier. https://www.olcf.ornl.gov/frontier, 2020.

[61] Jeremy Thomas. El Capitan. https://www.llnl.gov/news/llnl-and-hpe-partner-amd-el-capitan-projected-worlds-fastest-supercomputer, 2020.

[62] Jeffrey Slotnick, Abdollah Khodadoust, Juan Alonso, David Darmofal, William Gropp, Elizabeth Lurie, and Dimitri Mavriplis. CFD Vision 2030 Study: A Path to Revolutionary Computational Aerosciences. *NASA CR-2014-218178*, 2014.

[63] AMD. AMD EPYC 7742. https://www.amd.com/en/products/cpu/amd-epyc-7742, 2021. Last Accessed January 1, 2024.

[64] NVIDIA. NVIDIA H100 NVL Tensor Core GPU. https://resources.nvidia.com/en-us-tensor-core/nvidia-tensor-core-gpu-datasheet, 2023. Last Accessed January 1, 2024.

[65] NVIDIA Corporation. CUDA C Programming Guide. http://docs.nvidia.com/cuda/cuda-c-programming-guide, 2020. Last Accessed January 1, 2024.

[66] The OpenACC Organization. OpenACC. https://www.openacc.org, 2022. Last Accessed January 1, 2024.

[67] The OpenMP Consortium. The OpenMP API. https://www.openmp.org, 2020. Last Accessed January 1, 2024.

[68] John E Stone, David Gohara, and Guochun Shi. OpenCL: A parallel programming standard for heterogeneous computing systems. *Computing in Science & Engineering*, 12(3):66, 2010.

[69] AMD. AMD ROCm Platform. https://rocmdocs.amd.com/en/latest/, 2022. Last Accessed January 1, 2024.

[70] James Reinders, Ben Ashbaugh, James Brodman, Michael Kinsner, John Pennycook, and Xinmin Tian. *Data Parallel C++: Mastering DPC++ for Programming of Heterogeneous Systems Using C++ and SYCL*. Springer Nature, 2021.

[71] H Carter Edwards, Christian R Trott, and Daniel Sunderland. Kokkos: Enabling manycore performance portability through polymorphic memory access patterns. *Journal of Parallel and Distributed Computing*, 74(12):3202–3216, 2014.

[72] Richard D Hornung and Jeffrey A Keasler. *The RAJA Portability Layer: Overview and Status*. Lawrence Livermore National Lab.(LLNL), Livermore, CA (United States), 2014.

[73] The MPI Forum. The MPI Forum Website. `http://www.mpi-forum.org`, 2020. Last Accessed January 1, 2024.

[74] Hrvoje Jasak, Aleksandar Jemcov, Zeljko Tukovic, et al. OpenFOAM: A C++ library for complex physics simulations. In *International workshop on coupled methods in numerical dynamics*, volume 1000, pages 1–20, 2007.

[75] Kai Oßwald, Alexander Siegmund, Philipp Birken, Volker Hannemann, and Andreas Meister. L2Roe: a low dissipation version of Roe's approximate Riemann solver for low Mach numbers. *International Journal for Numerical Methods in Fluids*, 81(2):71–86, 2016.

[76] Brian Cantwell and Donald Coles. An experimental study of entrainment and transport in the turbulent near wake of a circular cylinder. *Journal of Fluid Mechanics*, 136:321–374, 1983.

[77] SG Goebel and JC Dutton. An experimental study of turbulent compressible mixing layers. *AIAA Journal*, 29(4):538–546, 1991.

[78] Joshua Codoni and Scott Berry. Analysis of dynamic data from supersonic retropropulsion experiments in NASA Langley's Unitary Plan Wind tunnel. In *42nd AIAA Fluid Dynamics Conference and Exhibit*, page 2706, 2012.

[79] Domenic D'Ambrosio, Giacomo Uffreduzzi, Adriano Pansini, and Roberto Marsilio. Numerical validation and analysis of supersonic retropropulsion test cases. In *AIAA Paper 2021-2868*, 2021.

[80] Ashley Korzun, Gabriel Nastac, Aaron Walden, Eric J Nielsen, William Jones, and Patrick Moran. Application of a detached eddy simulation approach with finite-rate chemistry to Mars-relevant retropropulsion operating environments. In *AIAA Paper 2022-2298*, 2022.

[81] Sanford Gordon and Bonnie J McBride. Computer Program for Calculation of Complex Chemical Equilibrium Compositions and Applications. Part 1: Analysis. *NASA RP 1311*, 1994.

[82] CO Johnston and AM Brandis. Modeling of nonequilibrium CO fourth-positive and CN violet emission in CO2–N2 gases. *Journal of Quantitative Spectroscopy and Radiative Transfer*, 149:303–317, 2014.

[83] Chul Park, John T Howe, Richard L Jaffe, and Graham V Candler. Review of chemical-kinetic problems of future NASA missions. II-Mars entries. *Journal of Thermophysics and Heat Transfer*, 8(1):9–23, 1994.

[84] Kazuhisa Fujita, Tetsuya Yamada, and Nobuaki Ishii. Impact of ablation gas kinetics on hyperbolic entry radiative heating. In *AIAA Paper 2006-1185*, 2006.

[85] Chul Park. *Nonequilibrium Hypersonic Aerothermodynamics*. Wiley, 1989.